J. Fluid Mech. (2007), *vol.* 588, *pp.* 279–308. © 2007 Cambridge University Press
doi:10.1017/S0022112007007562 Printed in the United Kingdom

Nonlinear resonances in a laminar wall jet: ejection of dipolar vortices

STEFAN WERNZ AND HERMANN F. FASEL
Department of Aerospace and Mechanical Engineering, The University of Arizona, Tucson, AZ 85721, USA

(Received 4 April 2006 and in revised form 18 May 2007)

Nonlinear mechanisms leading to the ejection of dipolar vortices from a laminar wall jet are being investigated using highly accurate Navier–Stokes simulations. With a set of well-defined numerical experiments for a forced Glauert wall jet, the nonlinear resonant interaction between the large-amplitude harmonic disturbance and a small-amplitude wave packet is systematically explored using two-dimensional simulations. Generated by a small-amplitude pulse, the wave packet experiences rapid resonant growth in the subharmonic part of its spectrum resulting in vortex mergings and, ultimately, the ejection of a pair of counter-rotating vortices from the wall jet. This two-dimensional subharmonic instability, if not mitigated by competing three-dimensional instabilities, can lead to the detachment of the entire wall jet from the surface. As shown using three-dimensional direct numerical simulations, vortex ejection still occurs in a forced transitional wall jet if the two-dimensional wave packet can reach a large amplitude level upstream of the region of three-dimensional turbulent breakdown. Movies are available with the online version of the paper.

1. Introduction

The ejection of dipolar vortices from a jet moving along a solid boundary (wall jet) is an intriguing dynamical process with profound implications for the development of the flow. On a large scale, kilometre-sized dipolar eddies have been detected in coastal currents (Ahlnäs, Royer & George 1987) transporting sediment-rich/warm water away from the coast. On a small scale, the formation of counter-rotating vortex pairs has been observed in laboratory experiments (Bajura & Catalano 1975) as part of the transition process in low-Reynolds-number laminar wall jets. In these experiments, a low-speed jet ($Re_j = 200$–600) was injected tangentially through a two-dimensional nozzle along the bottom wall of a water channel. Within ten nozzle-heights downstream of the nozzle, the flow developed into a self-similar laminar wall jet (Glauert 1956). The transition process was initiated by the emergence of two-dimensional instability waves that led to a double row of counter-rotating vortices, followed by one or several mergings of subsequent vortex pairs, lift-off of the vortex pairs from the wall, and three-dimensional turbulent breakdown immediately downstream of the vortex lift-off. In the unforced flow (natural transition), this process was intermittent and vortex mergings and subsequent lift-off occurred as random events separated by intervals of flow relaminarization. Harmonic forcing with acoustic disturbances considerably shortened the transition length and fixed the downstream location of vortex merging and vortex lift-off. For the unforced wall jet in particular, lift-off of the vortex pairs led to a temporary detachment of the flow from the channel wall. In technical wall-jet applications, especially for film-cooling, detachment from the surface would severely impair the operation of the jet and, at worst, could cause catastrophic device failure.

Large-amplitude dipolar vortices develop in laminar wall jets under various conditions. In the numerical simulations by Conlon & Lichter (1995) of transient planar wall jets penetrating into an initially quiescent enclosure, a starting dipole forms at the front of the jet, lifts off from the wall, and causes the jet to separate. Ejections of dipolar vortices also occur in two-dimensional simulations of a steady Glauert wall jet during start-up of harmonic forcing with large-amplitude blowing and suction (Wernz & Fasel 1996*a*, *b*), or in response to forcing with a large-amplitude pulse disturbance (Fasel & Wernz 1996). Common to all these cases is the formation of isolated, large-amplitude vortex dipoles that lift away from the wall through mutual induction of the two counter-rotating vortices constituting the dipoles. Different from the transient wall jet, the dipole in the steady wall jet emerges out of a downstream propagating two-dimensional wave packet that develops in response to the pulse disturbance or the sudden start-up of harmonic forcing.

It is well known from many experimental and theoretical investigations (e.g. Tsuji *et al.* 1977; Mele *et al.* 1986; Tumin & Aizatulin 1997), that the Glauert wall jet supports the growth of two hydrodynamic instability modes: a viscous mode (Tollmien–Schlichting type) originating from the inner region adjacent to the wall, and an inviscid mode (Kelvin–Helmholtz type) associated with the inflection point in the outer region. Each mode exhibits vorticity concentrations in both regions that, as the disturbance amplitude reaches saturation level, develop into the double vortex row observed in the experiments by Bajura & Catalano (1975), or in the two-dimensional numerical simulations by Wernz & Fasel (1996*a*). In the simulations, the forced flow converges to a time-harmonic state and, unlike in the experiments, no vortex ejections occur after the initial start-up of forcing. The flow becomes time-harmonic even if, in addition to large-amplitude forcing at a fundamental frequency, small-amplitude forcing at half that frequency is applied. As shown in the simulations by Wernz & Fasel (1996*a*) and later confirmed by Tumin (1998), the additional subharmonic disturbance in this case is strongly amplified through resonant interaction with the fundamental disturbance leading to the merging of subsequent vortex pairs farther downstream. Vortex merging in the experiments was immediately followed by vortex ejection, indicating that the merging may be a necessary precursor to the ejection by breaking the balance between subsequent vortex pairs within the double row. However, vortex merging alone is not sufficient. Our simulations have shown that the flow remains time-harmonic despite the merging. Evidently, an additional ingredient is required for triggering the ejection process. A strong candidate for this is the random background disturbance (noise, free-stream turbulence) that even in ‘clean’ experiments is orders of magnitude higher in amplitude than in our numerical simulations using high-order Navier–Stokes codes. However, random background perturbations also trigger competing three-dimensional instabilities leading to turbulent breakdown. This may be the reason why in experiments and simulations of wall jets at larger Reynolds numbers ($Re_j \gg 1\,000$) with a higher perturbation level, vortex mergings and vortex ejection have not been observed during transition (e.g. Levin *et al.* 2005).

In this paper, small-amplitude pulse disturbances are employed as a model for small two-dimensional perturbations that may be present in the natural flow. The impact of the wave packet generated by such a pulse disturbance on the forced wall jet is studied with a set of well-defined numerical experiments using two-dimensional Navier–Stokes simulations. The focus here is not on the actual ejection process

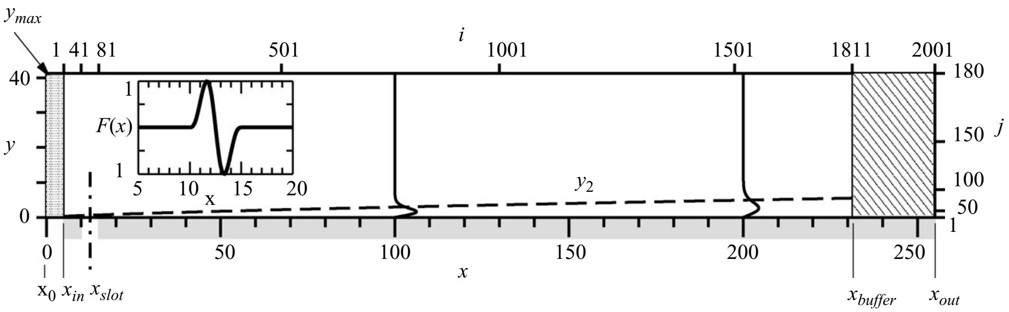

FIGURE 1. Computational domain indicating the location of the virtual origin of the wall jet, x_0, the domain inflow, x_{in}, the location of the forcing slot, x_{slot}, the beginning of the buffer domain, x_{buffer}, and the domain outflow, x_{out}. Grid point locations i,j are marked at the right-hand side and top of the domain. Also plotted are streamwise velocity profiles at $x = 100$ and $x = 200$ (—) and the half-width of the Glauert wall jet, y_2 (– – –). The inset shows forcing profile $F(x)$.

per se. Rather, emphasis is on the physical mechanisms acting farther upstream to strongly amplify non-periodic disturbances with a much smaller amplitude level than is required for triggering the ejections with a pulse disturbance alone. In addition, direct numerical simulations are employed to demonstrate that the wave-packet development and ejection process can still occur in a wall jet that transitions to turbulence.

2. Computational approach

For the present simulations, an incompressible Navier–Stokes code developed for direct numerical simulation (DNS) of boundary-layer transition (Meitz & Fasel 2000) has been adapted to the wall jet geometry (Wernz 2001). In this code, the Navier–Stokes equations in vorticity-velocity formulation are solved numerically using a fourth-order accurate Runge–Kutta method for the time integration and fourth-order compact differences in the streamwise and wall-normal directions. In three-dimensional simulations, a pseudo-spectral method with a Fourier decomposition in the spanwise direction is employed. For the present simulations, all flow quantities are non-dimensionalized with a reference velocity $U^* = 3\ \mathrm{m\ s^{-1}}$ and a reference length $L^* = 3.2$ mm; assuming for the kinematic viscosity $\nu^* = 1.5 \times 10^{-5}\ \mathrm{m^2\ s^{-1}}$ (air) the reference Reynolds number is $Re = 640$. For this chosen scaling, the non-dimensional thickness and streamwise mean velocity of the wall jet range is of the order of one throughout the domain of interest.

Figure 1 shows the computational domain extending in the streamwise direction from $x_{in} = 5$ to $x_{out} = 255$ with 2001 equidistant grid points. In the wall-normal direction, a variable grid is employed with 180 points that are clustered towards the wall (grid locations j are indicated in figure 1). For the three-dimensional simulations in §4, periodicity of the flow field is enforced in the spanwise direction with a fundamental spanwise wavelength of $L_z = 40$ (effective spanwise domain width). This direction is resolved using $K = 81$ full Fourier modes and 256 collocation points for computing the convective terms. The boundary conditions in the streamwise and wall-normal directions include Dirichlet conditions for the vorticity and velocity components at the inflow ($x_{in} = 5$), zero disturbances at the free-stream boundary ($y_{max} = 41.2$), and a buffer domain near the outflow boundary (from $x_{buffer} = 231.25$

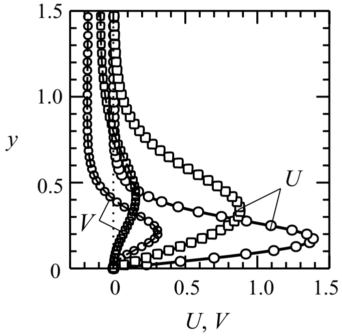

FIGURE 2. Glauert similarity solution employed as the base flow for the computations. Streamwise (U) and wall-normal (V) velocity profiles at $x_{in} = 5$ (○) and at $x_{slot} = 12.5$ (□).

Parameter	Value	Formula	Comment
U^*	$3\,\mathrm{m\,s^{-1}}$	—	Reference velocity
L^*	$3.2 \times 10^{-3}\,\mathrm{m}$	—	Reference length
ν^*	$1.5 \times 10^{-5}\,\mathrm{m^2\,s^{-1}}$	—	kinematic viscosity (air)
Re	640	$U^* L^* (\nu^*)^{-1}$	Reference Reynolds number
x_0	0	—	Virtual origin of wall jet
F^*	$1.6875 \times 10^{-5}\,\mathrm{m^5\,s^{-3}}$	$\int_0^\infty U^*(y^*) \int_{y^*}^\infty [U^*(\tilde{y})]^2 \mathrm{d}\tilde{y}\, \mathrm{d}y^*$	Flux of exterior mom. flux
P_{y2}	9.30497×10^{-2}	$5.88498\,(\nu^*)^{3/4}(F^* L^*)^{-1/4}$	Parameter in (2.1)
P_{Um}	3.11267	$0.49803\,(F^*)^{1/2}(\nu^* L^*)^{-1/2}(U^*)^{-1}$	Parameter in (2.2)

TABLE 1. Important flow parameters for the present simulations.

to $x_{out} = 255$) for relaminarizing the flow (see Meitz & Fasel 2000). At the wall, the velocity components are set to zero, except for the wall-normal velocity component over the forcing slot near the inflow.

In a precursor calculation, a steady two-dimensional base flow is computed which closely matches the similarity solution by Glauert (1956) but, of course, satisfies the discretized Navier–Stokes equations. To ensure that the base flow is independent of the computational domain height, special care must be taken to recover the induced flow field of the wall jet far away from the wall, where the similarity solution is invalid. This is achieved by imposing flow profiles at the inflow that combine the similarity solution near the wall with an asymptotically matched potential flow solution away from the wall (Wernz 2001). The self-similar Glauert wall jet has its virtual origin at $x_0 = 0$ and has a strength that is characterized by the flux of the exterior momentum flux, F^*, which remains constant over x. The resulting velocity profiles at the inflow and at the forcing slot are plotted in figure 2.

Table 1 gives the base-flow parameters and reference scales chosen for the present simulations. Since no experimental measurements are available for a direct comparison with the present simulation data, the same flow parameters and reference scales are used as in our earlier wall-jet investigations (Wernz & Fasel 1996*a*, 1997, 2000; Wernz 2001). (The Glauert wall jet employed as a base flow for the present and earlier simulations was matched up with the nearly self-similar laminar wall jet from nonlinear instability experiments in air by Zhou, Rothstein & Wygnanski (1992). In the experiments, the wall jet issued from a nozzle of width b = 3.2 mm with an exit velocity of $U_j = 2$ m s^{-1} and approached a self-similar Glauert wall jet with $F^* = 1.6875 \times 10^{-5}$ m^5 s^{-3} within $\approx 8\,b$ downstream of the nozzle exit.) All flow variables can be easily rescaled using the following relations for the streamwise development of the local half-width, y_2, and streamwise velocity maximum, U_m, of the Glauert wall jet,

$$y_2 = P_{y2}(x - x_0)^{3/4}, \tag{2.1}$$

$$U_m = P_{Um}(x - x_0)^{-1/2}, \tag{2.2}$$

where the parameters P_{y2} and P_{Um} are also given in table 1 for the particular flow here. Therefore, for any streamwise location x, the local Reynolds number of the wall jet computes as

$$Re_{y2} = Re\, U_m\, y_2 = Re\, P_{y2} P_{Um}(x - x_0)^{1/4}\,. \tag{2.3}$$

2.1. *Forcing method*

In the Navier–Stokes simulations, harmonic and/or pulse disturbances are introduced into the base flow by simultaneous wall-normal blowing and suction through a slot in the wall centred at $x_{slot} = 12.5$. This technique is efficient for producing vortical disturbances while minimizing acoustic disturbances. The slot velocity is computed as

$$v_s(x, y = 0, t) = F(x)[A_h \cos(2\pi f_h t) + A_p T_p(t)], \tag{2.4}$$

where $F(x)$ represents the shape of the blowing and suction profile (insert in figure 1), A_h and f_h are amplitude and frequency of the time-harmonic disturbance, and A_p is the amplitude of the pulse disturbance. The time function of the pulse is given by

$$T_p(t) = [H(t - t_p) - H(t - t_p - \Delta t_p)] \sin^6(\pi t/\Delta t_p) \cos(2\pi f_p t), \tag{2.5}$$

where $H(t)$ is the Heaviside step function, t_p the start of the pulse in time, Δt_p the pulse width, and f_p the carrier frequency of the pulse. Note, the phase angle of the time-harmonic disturbance at time t_p,

$$\theta_{h,p} = \theta_h(t_p) = 2\pi\{f_h t_p\}, \tag{2.6}$$

can, in some cases, have a significant effect on the growth behaviour of the generated disturbance. The disturbance frequencies, f_h and f_p, and the pulse width, Δt_p, are non-dimensionalized by a reference frequency, $f^*_{ref} = 56$ Hz, which was chosen as the frequency of the fundamental harmonic disturbance in the present simulations and matches the forcing frequency in one case from the experiments by Zhou *et al.* (1992). Time functions for three pulse disturbances are plotted in figure 3(*a*) versus time and in figure 3(*b*) versus frequency (Fourier transformed). This particular form of function T_p was chosen here because: (i) the pulse duration is finite without the need for artificial clipping (as opposed to a Gaussian); (ii) the spectral content of the pulse can be limited to a chosen frequency band with few parameters. Function T_p is designed such that the main frequency band of the pulse is centred around f_p with a width of $\Delta f_b \leqslant 8/\Delta t_p$. The sharp drop in amplitude for the undesirable frequency side bands is achieved by furnishing the sine function in (2.5) with a high exponent.

For the three-dimensional simulations in §4, forcing with random white noise is applied in all Fourier components, k, for tripping the flow to turbulence,

$$v_r(x, y = 0, k, t) = F(x) A_r T_r(t, k)\,, \tag{2.7}$$

where A_r is the forcing amplitude. Function $T_r(t, k) \epsilon [-1, 1]$ is provided by a white noise generator called at every computational time step and for each Fourier component.

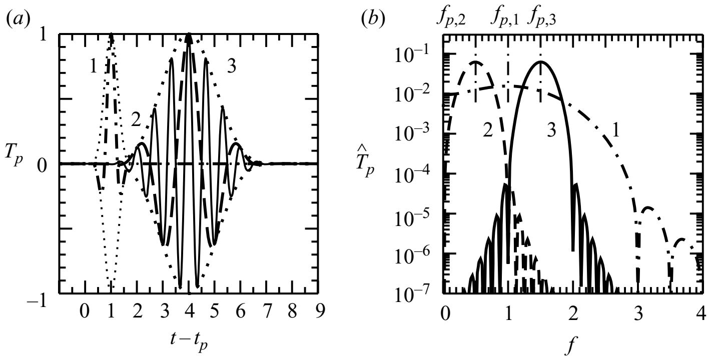

FIGURE 3. Time functions for three pulse disturbances. (*a*) Pulse disturbances versus time. (*b*) Frequency spectra for the pulse disturbances. Pulse type 1: short duration pulse (– · –); pulse type 2: low-frequency pulse (– – –); pulse type 3: high-frequency pulse (—). Note, a sampling period of $\Delta t = 40$ is used for computing the spectra from the time functions.

2.2. *Validation*

The DNS code has been validated extensively by Meitz & Fasel (2000). For the DNS of wall jets, grid convergence studies have ensured that the influence of the discretization error on the flow solution is kept small. In particular, since the present two-dimensional simulations are inexpensive to run on current high-performance computers, the grid has been oversized in terms of grid resolution and domain size. Specifically, more than 32 points are employed per wavelength of the fundamental disturbance and the computational domain extends far away from the wall and far downstream (see figure 1). In addition, base flow and time-periodic flow have been converged for dozens of flow-through times until residual non-periodic disturbances generated during start-up have decreased in amplitude down to nine orders of magnitude below base-flow level. This was done to ensure that these uncontrolled disturbances do not interfere with the deliberately input pulse disturbance.

3. Two-dimensional simulation results

With a series of high-resolution two-dimensional simulations, the mechanisms responsible for the ejection of dipolar vortices from a Glauert wall jet have been studied. A well-defined pulse disturbance with a time behaviour that is described by (2.5) is employed as a prototypical disturbance to model the effect of small-amplitude two-dimensional random perturbations. The forcing parameters for the different simulation cases are given in table 2.

3.1. *Steady wall jet perturbed by small-amplitude pulse*

For Case 1, using small-amplitude blowing and suction, a pulse disturbance has been introduced into the laminar wall jet leading to the development of a downstream-travelling wave packet. The forcing amplitude was chosen small enough that nonlinear effects are negligible and the development of the wave packet is described well by linear stability theory. Owing to the short pulse duration, $\Delta t_p = 2$, the frequency spectrum of the pulse is very broad (see figure 3(*b*), pulse type 1) and, as a result, the ensuing wave packet also contains a wide range of frequencies. This is seen from the contour plot in figure 4 which plots the frequency spectrum of the wave packet versus downstream distance. A sampling period of $\Delta t = 40$

	A_h	f_h	A_p	f_p	Δt_p	$\theta_{h,p}$	Pulse type	Comment
Case 1	—	—	10^{-4}	1	2	0	1	Small-amplitude broad-spectrum pulse
Case 2	5×10^{-3}	1	—	—	—	—	—	Large-amplitude harmonic forcing
Case 3	5×10^{-3}	1	10^{-4}	1	2	0	1	Harmonic forcing + broad-spectrum pulse
Case 4	5×10^{-3}	1	10^{-5}	1	2	0	1	Harmonic forcing + smaller-amplitude pulse
Case 5	5×10^{-3}	1	10^{-3}	1	2	0	1	Harmonic forcing + larger-amplitude pulse
Case 6	5×10^{-3}	1	10^{-4}	0.5	8	0	2	Harmonic forcing + low-frequency pulse
Case 7	5×10^{-3}	1	10^{-4}	1.5	8	0	3	Harmonic forcing + high-frequency pulse
Case 8	2×10^{-2}	1	10^{-4}	1	2	0	1	Large-amplitude harmonic forcing + broad-spectrum pulse
Case 9	2×10^{-2}	1	10^{-4}	1	2	π	1	Phase shifted harmonic forcing + broad-spectrum pulse
Case L	5×10^{-3}	1	10^{-6}	1	2	0	1	Harmonic forcing + very small-amplitude pulse
Case P	—	—	10^{-2}	1	2	0	1	Large-amplitude broad-spectrum pulse
Case S	—	—	—	—	—	—	—	Start-up of steady blowing

TABLE 2. Forcing parameters for simulation cases. For an illustration of the time-behaviour and the frequency spectra of pulse types 1–3 see figure 3. Note, f_h, f_p and Δt_p are normalized by the reference frequency, $f^*_{ref} = 56$ Hz. Phase angle, $\theta_{h,p}$, has been defined in (2.6).

is used for the Fourier transform. For reference, the neutral curves of the viscous inner mode and the inviscid outer mode according to linear stability theory (LST) are also shown. The neutral curves have been renormalized using (2.1)–(2.3) from the local coordinates (Re_{y2}, β) that are typically used in the literature (the local frequency, β, relates to frequency f as $\beta = P_\beta \, U_m^{-1} \, y_2 \, f$ with $P_\beta = 2\pi \, f^*_{ref} \, U^{*-1} \, L^*$) for plotting the linear stability diagram of the wall jet (see inset in figure 4; see also, e.g. Tsuji *et al.* 1977; Tumin & Aizatulin 1997). Close to the forcing slot (receptivity region) where the disturbance is still adjusting and where both linear instability modes are present simultaneously, a comparison between simulation data and LST results is difficult. Farther downstream, however, the location where the inner mode reaches its maximum amplitude (marked in figure 4 with white dashed line) coincides remarkably well with branch two of the neutral curve from LST over a wide frequency range. This is an indication that the wave packet is a true linear superposition of harmonic disturbances, a fact that is further demonstrated in figure 5. Shown in figure 5(*a*) is the amplitude development of selected frequency components within the wave packet in comparison with the corresponding harmonic disturbances (each computed in a separate Navier–Stokes simulation) at these same frequencies. The match between wave packet and harmonic disturbances is nearly perfect, except for the slight discrepancy observed for the curves corresponding to $f = 1/2$. A perfect match is observed in figure 5(*b*) between the normalized disturbance profile from the frequency component, $f = 1$, within the wave packet, the profile of a harmonic disturbance of $f_h = 1$, and the eigenfunction from LST for $f_h = 1$, all three at $x = 55$. Notice from the semi-logarithmic plot in figure 5(*a*),

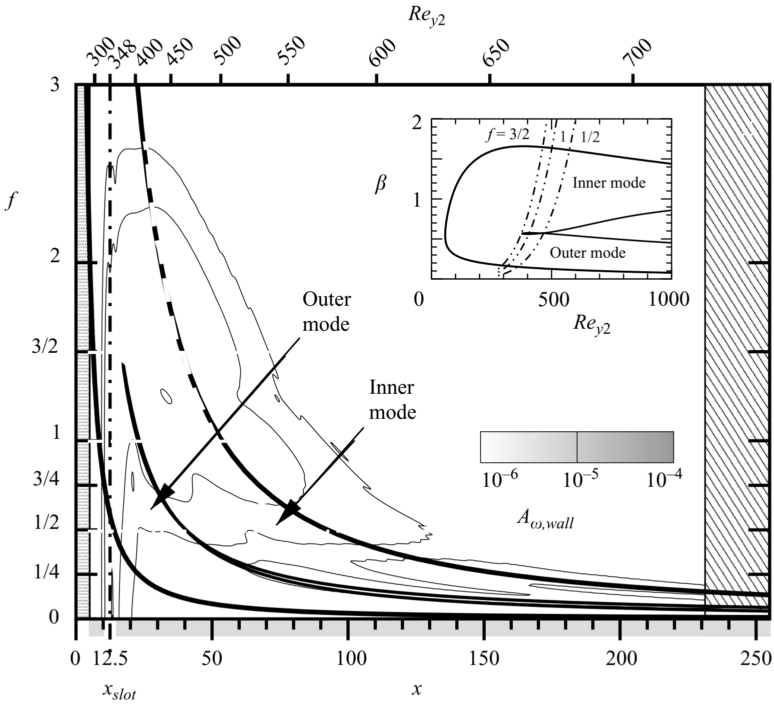

FIGURE 4. Linear development of a small-amplitude wave packet generated by pulse disturbance (Case 1). Contour plot of the Fourier amplitude $A_{\omega,wall}$ in logarithmic scale versus frequency f and streamwise distance x. The local Reynolds number Re_{y2} is also marked at the top of the graph. Plotted for comparison are the neutral curves (—) according to LST. Inset: Paths of disturbances with constant frequency f (–··–) in the linear stability diagram with the neutral curves plotted versus local frequency, β, and Reynolds number, Re_{y2}.

that the amplitude increase of the wave packet in the downstream direction owing to linear amplification is less than one order of magnitude and the disturbance amplitude remains far below the nonlinear saturation level. As a result, the wave packet propagates throughout the integration domain while first growing, then decaying without any lasting effect on the base flow.

3.2. *Wall jet perturbed by large-amplitude time-harmonic forcing*

As reported by Wernz & Fasel (1996*a*), time-harmonic forcing of the wall jet with a large amplitude may lead to the ejection of dipolar vortices during start-up. Yet in our simulations, a time-harmonic state of the forced flow could still be reached using one of three approaches: (i) by computing over a very long transient time-period after the initial vortex ejection, (ii) by gradually ramping up the forcing amplitude over time, thus reducing the amplitude of the start-up wave packet, or (iii) by slowly moving the outflow buffer in the downstream direction at a lower rate than the propagation speed of the start-up wave packet, which is thus ‘killed off’ by the buffer.

In Case 2, the wall jet is harmonically forced with frequency, $f_h = 1$, and with an amplitude, $A_h = 5 \times 10^{-3}$, that is 50 times larger than the amplitude, A_p, of the pulse in Case 1. Note, however, A_h is still ≈200 times smaller than the streamwise velocity maximum of the base flow at the forcing location (figure 2). The forced wall jet in Case 2 has been converged towards a time-periodic state until non-periodic

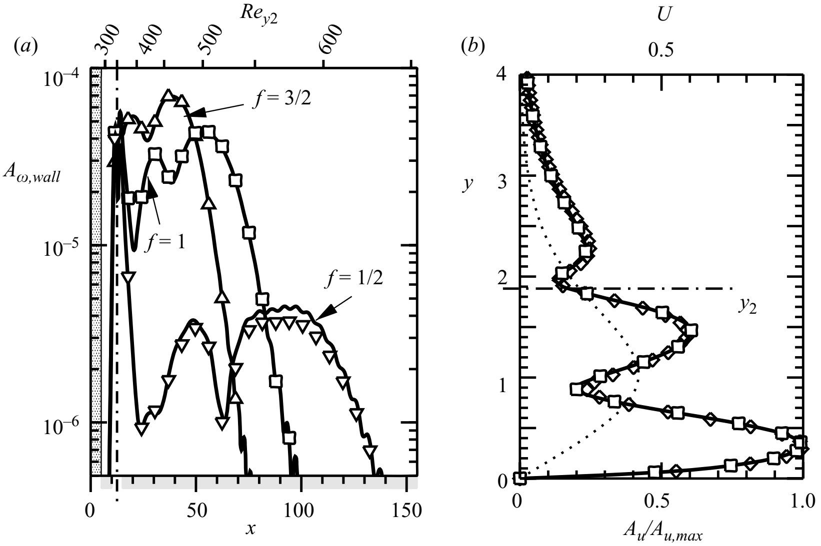

FIGURE 5. Comparison of small-amplitude wave packet generated by pulse disturbance (Case 1) with harmonic disturbances. (*a*) Disturbance amplitudes (wall-vorticity) versus x for selected frequencies within the Fourier spectrum (lines) compared to harmonic disturbances with the same frequencies (symbols). (*b*) Amplitude profiles (streamwise velocity) for $f = 1, x = 55$ where (—) is obtained from the wave packet, (□) from a harmonic disturbance, and (◇) from LST, (···) represents the local mean velocity profile.

disturbances within the flow field have decayed down to more than eight orders of magnitude below forcing level. Figure 6 illustrates the downstream development of the large-amplitude harmonic disturbance. The disturbance amplitude represented by the wall-vorticity fluctuations, $A_{\omega,wall}$, is plotted in figure 6(*a*) versus x (here on a linear scale) while the amplitude profile of the streamwise disturbance velocity at $x = 55$ is shown in figure 6(*b*). For reference, the base flow and the corresponding curves from a linear calculation ($f_h = 1$, $A_h = 10^{-4}$) are also plotted. For better comparison, the amplitude of the linear disturbance in both figures 6(*a*) and 6(*b*) is multiplied by a factor of 50 so that the disturbance amplitude from Case 2 is matched at the forcing location. Clearly, the nonlinear disturbance from Case 2 reaches a significant amplitude level when compared to the base flow. In the wall vorticity (figure 6*a*), the maximum amplitude of the nonlinear disturbance is reached at $x \approx 55$ matching the wall vorticity of the base flow. For the streamwise velocity profile at $x = 55$ (figure 6*b*), the amplitude maximum in the near-wall region is at approximately 15% of the local velocity maximum of the base flow. As illustrated by the contour plot of instantaneous vorticity inserted in figure 6(*b*), the nonlinear disturbance from Case 2 forms a double-vortex row that has vorticity concentrations with counterclockwise rotation in the outer region and clockwise rotation near the wall. Within the 'low-noise environment' of our numerical simulations, the forced wall jet in Case 2 remains at a time-harmonic state despite the large amplitude of the disturbance present in the flow. The question that arises now is what happens when the forcing from Cases 1 and 2 is combined.

3.3. *Forced wall jet perturbed by small-amplitude pulse*

In Case 3, the forced wall jet from Case 2 is subjected to additional forcing at time t_p with a small-amplitude pulse that is identical to the pulse in Case 1. Figure 7

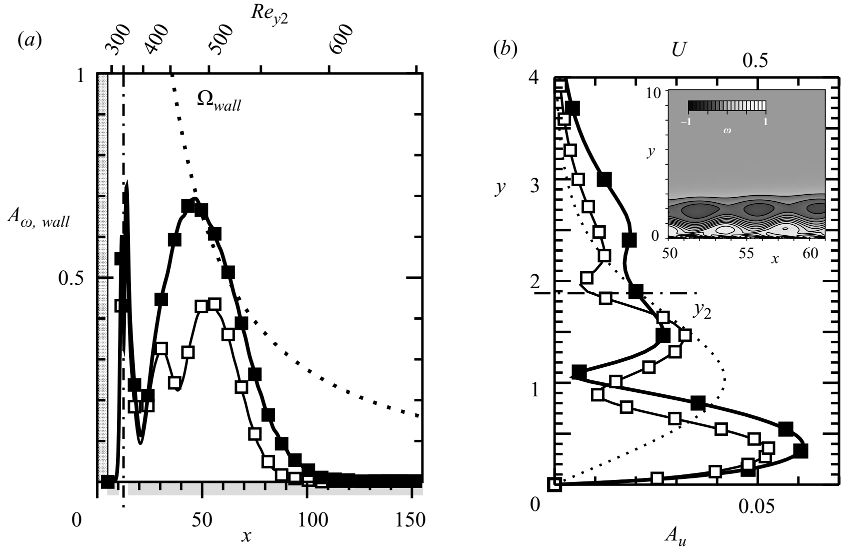

FIGURE 6. Nonlinear development of large-amplitude time-harmonic disturbance with frequency $f_h = 1$ (Case 2). Comparison with linear disturbance of the same frequency. (*a*) Disturbance amplitudes (wall-vorticity) versus x; (*b*) amplitude profiles (streamwise velocity) at $x = 55$. Large-amplitude disturbance represented by curves marked with (■), small-amplitude disturbance marked by (□) (note, disturbance amplitude multiplied by factor of 50 for better comparison), base flow represented by (···).

shows the flow field represented by spanwise vorticity at four successive time instants after the pulse has been applied. Whereas in figure 7(*a*), ten fundamental forcing periods after pulse deployment, the effect of the downstream propagating wave packet on the flow is still not visible, ten periods later in figure 7(*b*) the wave packet has grown to a large amplitude while significantly altering the double vortex row downstream of $x = 70$. At this time instant, two subsequent vortex pairs are in the process of merging at $x \approx 75$ near the tail end of the wave packet. Another ten periods later (figure 7(*c*)), a dipolar vortex pair has just lifted away from the wall. Forty periods after the pulsed forcing (figure 7(*d*)), the dipole has propelled itself far up into the quiescent region above the wall jet through mutual induction of the two counter-rotating vortices. As is most often the case, the circulation associated with the vortex of counterclockwise rotation (originating from the outer region of the wall jet) is greater than that of the vortex of clockwise rotation (from the inner region) and, as a result, the vortex dipole moves in a curved path in the upstream direction. At a later time, owing to the entrainment by the wall jet, the dipole will be re-ingested by the wall layer, leading to a secondary vortex ejection (not shown) similar to the process observed by Wernz & Fasel (1996*b*) during the start-up of harmonic forcing.

3.4. *Ejection scenarios*

The ejection process from Case 3 can be captured in its entirety within a single plot by using iso-surfaces of vorticity as a function of streamwise and wall-normal location, and time (figure 8(*a*)). In particular, the curved trajectory of the vortex dipole lifting off from the wall and the sequence of vortex mergings in the outer shear layer before and during the lift-off can be readily observed. Figure 8 also

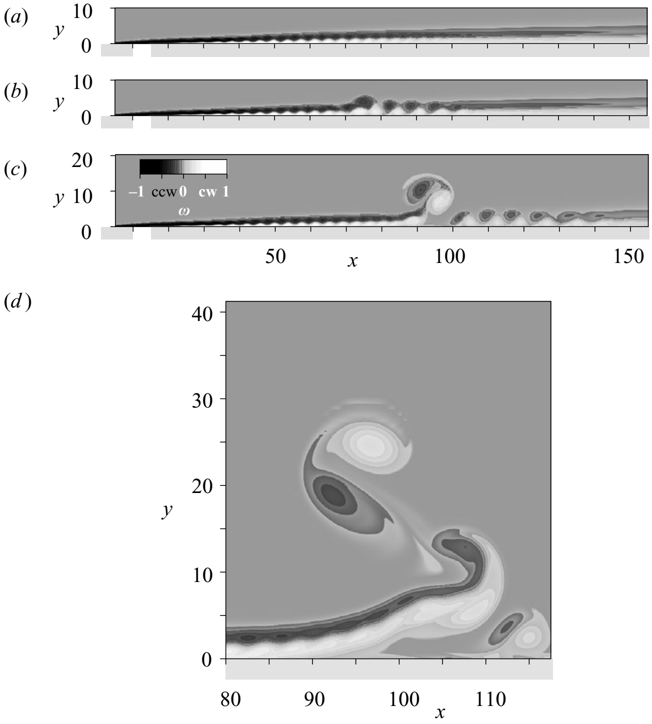

FIGURE 7. Ejection of vortex dipole from a forced wall jet in response to pulse disturbance (Case 3). Shown are grey-scales of vorticity at four time instants: (*a*) $t_p + 10$, (*b*) $t_p + 20$, (*c*) $t_p + 30$, and (*d*) $t_p + 40$. The ejection process is also visualized in movie 1 available with the online version of the paper.

provides a compilation of different flow scenarios where vortex ejections are triggered by various types of perturbations. Many features of this prototypical Case 3 are also shared by the other three scenarios shown in figure 8. Figure 8(*b*) illustrates the start-up of harmonic forcing which, after a long time-duration, will lead to the time-periodic flow of Case 2. The ejection occurring during the start-up is also preceded by vortex mergings and the ejected vortex dipole moves upstream in a curved path. For Case P in figure 8(*c*), the flow is forced with a short-duration pulse that is identical in shape to the pulse from Case 1, but has an amplitude a 100 times larger. In this case, no vortex mergings are observed ahead of the ejection process. The compact wave packet generated by the large-amplitude pulse already contains a vortex pair that is energetic enough to lift off from the wall and lacks strong enough neighbouring pairs to prevent the lift-off. Finally, figure 8(*d*) shows the start-up of blowing at a shallow angle through a slot in the wall (Case S). The flow in this case, although profoundly disturbed during start-up, converges over time to an attached laminar wall jet with the shape of a Glauert profile.

3.5. *Development of the wave packet in the forced wall jet*

It is important to note that for Cases 2 and P (figures 8(*b*) and 8(*c*)) the non-periodic perturbation introduced into the flow is very strong. As a result, the downstream travelling wave packet that precedes the ejection process already has a large nonlinear amplitude from the time of its generation. For the forced wall jet in Case 3, on the

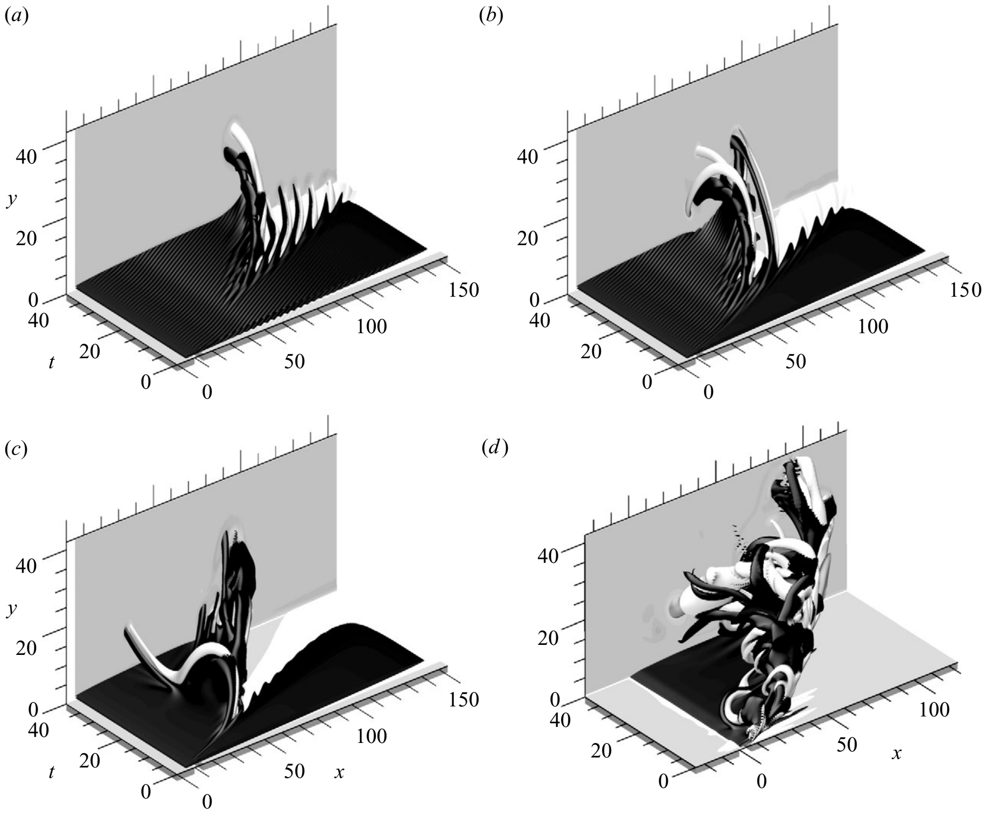

FIGURE 8. Compilation of ejection scenarios. Shown are iso-surfaces of vorticity with clockwise (light) and counter-clockwise (dark) rotation plotted versus x, y and t. (a) Harmonic forcing + pulse (Case 3); (b) start-up of harmonic forcing (Case 2); (c) large-amplitude pulse (Case P); (d) start-up of blowing through slot (Case S). Forcing parameters are given in table 2.

other hand, a minute pulse disturbance appears to be sufficient to start the process. How can a pulse of such small amplitude disrupt the forced wall jet in such a dramatic manner while having virtually no effect on the unforced jet? An excellent starting point for finding an answer to this question is a close examination of the wall vorticity, ω_{wall}, the footprint on the wall left by the vortical disturbances inside the flow field. In figure 9(a), ω_{wall} is plotted versus x and t in a space–time diagram. The dark and light lines are fluctuations in ω_{wall} tracing the downstream-propagating disturbances over time. For the first ten fundamental forcing periods after the pulse has been introduced, the flow field still appears time-harmonic. Then, at time $t \approx t_p + 15$ and $x \approx 60$, a merging of subsequent dark lines (representing counterclockwise wall vorticity) is observed reflecting the vortex mergings that take place inside the flow. After a second merging at $t \approx t_p + 21$ and $x \approx 80$, a negative spike in the wall vorticity (counterclockwise rotation) is observed within the area marked by the dashed box. A close-up of the flow region near the vorticity spike is provided in figure 9(b) with snapshots of the flow field and the corresponding wall vorticity at three time-instants during the vortex ejection process. As the vortex dipole lifts up from the wall, the wall vorticity locally decreases, reaches a minimum at $t \approx t_p + 23$ and $x \approx 85$ and

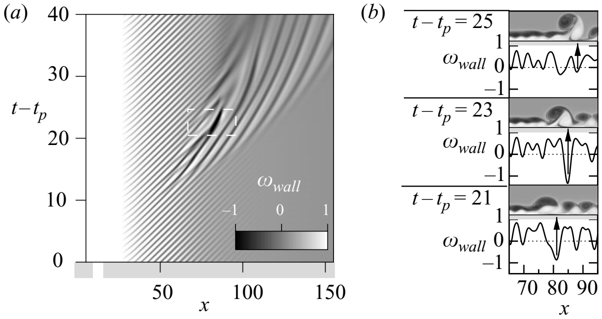

FIGURE 9. Downstream development of a wave packet in the forced wall jet from Case 3: (*a*) space–time diagram for the wall vorticity; (*b*) close-up of dipole lift-off showing grey-scales of vorticity and corresponding wall vorticity at time $t - t_p = 21, 23, 25$. Arrows mark the location of the negative vorticity spike indicating lift-off.

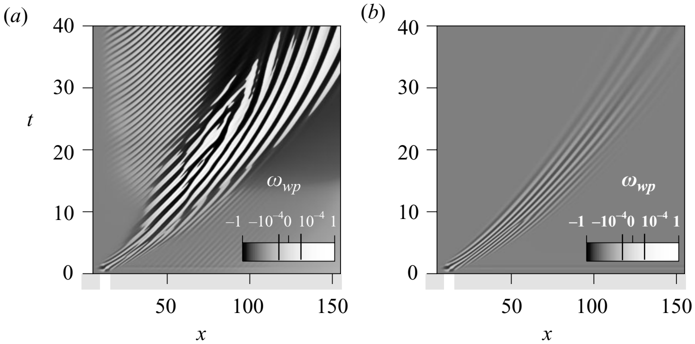

FIGURE 10. Development of the wave packet in the forced and in the unforced wall jet. Space–time diagrams for the wall vorticity attributed to the wave packet only. Base flow and time-periodic disturbances are subtracted from the signal, grey-scale contours of vorticity are plotted on a logarithmic scale. (*a*) Case 3 (forced), (*b*) Case 1 (unforced).

then increases again. Incidentally, this negative spike in ω_{wall} was also observed by Conlon & Lichter (1995) during the dipole lift-off in a transient wall jet.

From the direct comparison of Cases 1 and 3 in figure 10, a true appreciation can be gained of the tremendous difference between the development of a wave packet in the forced and in the unforced wall jet. Figure 10 shows space–time diagrams for the wall vorticity attributed to the wave packet, $\omega_{wp,wall}$ (with the wall vorticity of the base flow, and for Case 3 also the time-harmonic disturbance, subtracted out). For $|\omega_{wp,wall}| > 10^{-4}$, the plotting scale is logarithmic which allows for illustrating disturbance growth over many orders of magnitude within one grey-scale plot. Note, in both cases the flow is perturbed with the identical small-amplitude pulse disturbance and, as a result, the wall vorticity in figures 10(*a*) and 10(*b*) appears identical in the vicinity of the forcing slot. Farther downstream, however, the wave packet in Case 3 grows by more than three orders of magnitude, while in Case 1 the amplitude of the wave packet remains small. For time $t > 30 + t_p$, the flow upstream of $x \approx 80$ returns to a time-harmonic state, although with a slight phase shift that is noticeable in figure 10(*a*). Downstream of $x \approx 80$, fluctuations associated with the wave packet remain strong throughout the remainder of the time period covered in figure 10(*a*).

3.6. *Nonlinear resonances in the forced wall jet*

The fact that ω_{wall} at $t = t_p$ and at $t = t_p + 40$ (almost) match upstream of $x = 80$, allows for a Fourier transform in time without the need for windowing to counteract otherwise occurring end effects. The frequency spectrum obtained from the transform (a sampling period of $\Delta t = 40$ is used) is plotted in figure 11(*a*) for locations upstream of $x = 90$. The spectrum for Case 3 in figure 11(*a*) differs greatly from the corresponding spectrum for Case 1 in figure 4. The Fourier amplitude, $A_{\omega,wall}$, for Case 3 ranges over four orders of magnitude with discrete peaks at the fundamental forcing frequency, $f = 1$, and its higher harmonics, $f = 2, 3, 4$, which are attributed to the large-amplitude harmonic disturbance. Note, the amplification observed for frequencies around $f = 1/2$ and $f = 3/2$ is remarkable: The disturbance growth ranges over three orders of magnitude from the amplitude level over the blowing and suction slot up to saturation level downstream of $x = 50$. A direct comparison between Cases 1 and 3 is made in figure 11(*b*), plotting the Fourier amplitude of the wall vorticity versus x for frequencies $f = 1/4$, $1/2$, 1 and $3/2$. The corresponding amplitude curves from Case 3 (solid lines) and Case 1 (dotted lines) match up for a short distance downstream of the forcing slot, indicating that these Fourier components initially develop linearly. At the forcing location, the disturbance is amplified for $f = 3/2$ and damped for $f = 1/2$ and $f = 1/4$ according to linear theory, as seen from figure 4. However, starting at $x \approx 20$, the amplitude curves from Case 3 for $f = 1/2$ deviate from their respective linear behaviour and start to grow rapidly. The strongest growth is experienced by the subharmonic, $f = 1/2$, which surpasses the amplitude of component $f = 3/2$ downstream of $x = 35$. This rapid subharmonic growth is the hallmark of a nonlinear resonance between the large-amplitude fundamental and the small-amplitude subharmonic disturbance, as was observed by Wernz & Fasel (1996*a*) and by Tumin (1998) for purely time-harmonic disturbances. The large-amplitude fundamental disturbance acts as a nonlinear amplifier for the small-amplitude non-periodic wave packet. Note, in figure 11(*b*) the nonlinear saturation level of the frequency components within the wave packet from Case 3 appears to remain far below the amplitude of the harmonic fundamental disturbance. The reason for this is that the pulse disturbance and the ensuing wave packet are localized in time (here $\Delta t_p = 2$) and the amplitude of the frequency spectrum associated with the pulse/wave packet scales with the much larger sampling interval of the Fourier transform (here chosen as $\Delta t = 40$). When rescaled by a factor of 20, the amplitude of the subharmonic Fourier component in Case 3 approaches that of the fundamental at $x \approx 70$, approximately the location where the first vortex merging is observed in the space–time diagram of figure 9 (at $t - t_p \approx 15$). A little farther downstream, the second subharmonic, $f = 1/4$, also reaches saturation and surpasses the subharmonic, $f = 1/2$, in amplitude. This leads to the second vortex merging observed in figure 9 at $x \approx 85$ ($t - t_p \approx 23$).

3.6.1. *Effect of pulse amplitude on the development of the wave packet*

Several parameter studies have been performed to determine whether the strong amplification of the wave packet in the forced wall jet is truly caused by a secondary instability. For example, according to Floquet theory of (weakly) nonlinear periodic shear flows, the growth rate of a small-amplitude secondary disturbance that is amplified owing to the presence of a large-amplitude primary disturbance, does not depend on the amplitude of the secondary disturbance. This expected linear growth behaviour has been verified by varying the amplitude, A_p, of the pulse from Case 3 while keeping its shape fixed (pulse type 1 from figure 3(*b*)). Results from this study

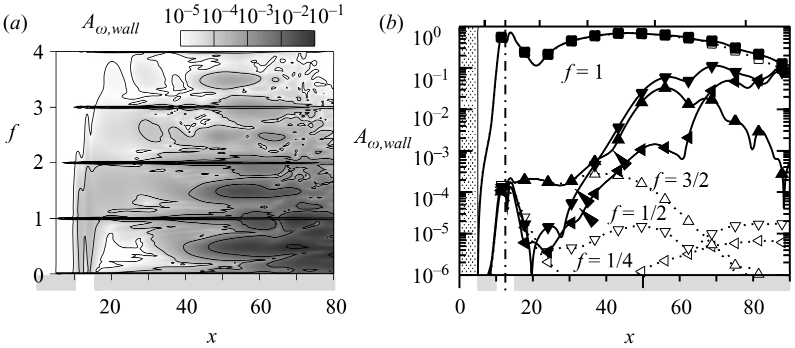

FIGURE 11. Downstream development of the wave packet in the forced wall jet (Case 3). (*a*) Fourier spectrum of the wall vorticity over x; (*b*) Fourier amplitude versus x for selected frequencies, $f = 1/4$ (◁); $f = 1/2$ (∇); $f = 1$ (□); $f = 3/2$ (△); Case 3, solid lines/filled symbols; also shown for comparison are Case 2, dotted line/open squares; and Case 1, dotted lines/open symbols.

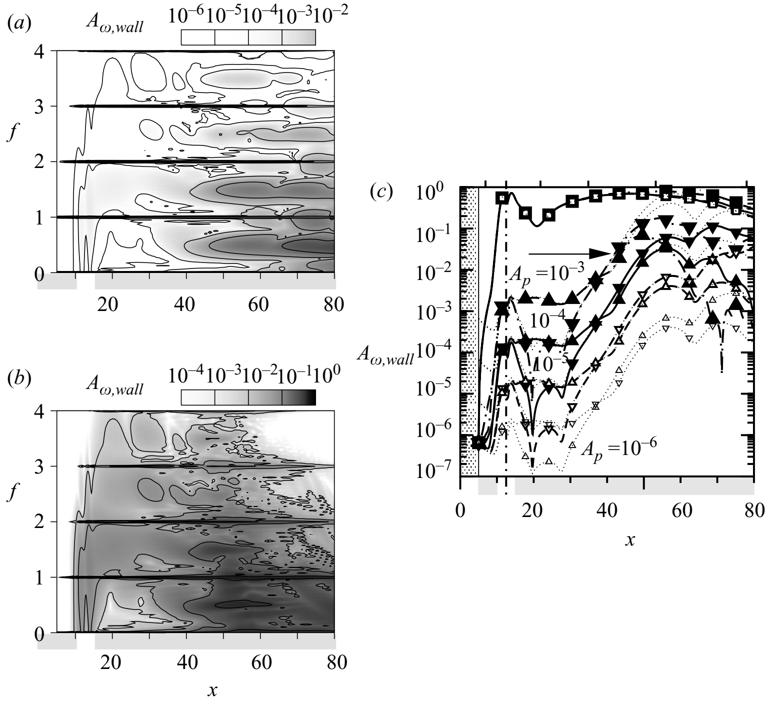

FIGURE 12. Dependence of wave packet development on the amplitude of the pulse. (*a*) Fourier spectrum for Case 4 ($A_p = 10^{-5}$); (*b*) Fourier spectrum for Case 5 ($A_p = 10^{-3}$); (*c*) Fourier amplitude versus x for selected frequencies, $f = 1/2$ (∇); $f = 1$(□); $f = 3/2$ (△); and pulse amplitudes, $A_p = 10^{-6}$/Case L (· · ·); $A_p = 10^{-5}$/Case 4 (– – –); $A_p = 10^{-4}$/Case 3 (—); $A_p = 10^{-3}$/Case 5 (—·—). Shown is the Fourier amplitude of the wall vorticity. Note, amplitude curves for Case L are also shown rescaled (· · ·, without symbols) to reveal deviation from linear behaviour for Cases 3–5. The arrow shows saturation onset.

are presented in figure 12. Shown in figure 12(*a*) is the Fourier spectrum of a wave packet generated by a pulse with $A_p = 10^{-5}$ (Case 4, table 2), an order of magnitude smaller than the amplitude of the pulse in Case 3. A comparison of figure 12(*a*) with figure 11(*a*) reveals that the amplitude growth of the wave packet in Cases 3 and 4 is virtually identical upstream of $x \approx 50$. Farther downstream, the Fourier spectrum for Case 3 reaches saturation while the spectrum of the smaller-amplitude pulse in Case 4 continues to increase in amplitude. On the other hand, when the pulse amplitude is increased to $A_p = 10^{-3}$ (Case 5, table 2), the Fourier spectrum of the pulse reaches saturation level farther upstream at $x \approx 40$, as seen from figure 12(*b*).

Figure 12(*c*) provides a quantitative comparison of the disturbance growth in Cases 3, 4 and 5 for selected frequency components within the wave packet ($f = 1/2$, $3/2$). Serving as a reference is Case L with $A_p = 10^{-6}$, where the amplitude of the wave packet remains well below the nonlinear saturation level throughout the computational domain. In figure 12(*c*), the amplitude curves from linear Case L (marked by the dotted lines) have been rescaled such that over the blowing and suction slot these rescaled curves match the corresponding curves from each of the other three cases. Departure of the amplitude growth in Cases 3–5 from that in Case L therefore indicates the onset of nonlinear saturation in these cases. While Case 4 shows no noticeable difference to Case L and thus exhibits linear secondary growth throughout the streamwise domain shown, nonlinear saturation sets in at $x \approx 50$ for Case 3 and at $x \approx 40$ for Case 5. Not surprisingly, the amplitude of the pulse disturbance determines the streamwise location where the wave packet reaches saturation and begins to disrupt the forced wall jet.

3.6.2. *Low-frequency versus high-frequency pulse*

The numerical experiment of Case 3 demonstrates that in response to forcing with a broad-spectrum pulse, subharmonic disturbances of $f \approx 1/2$ are the most amplified owing to resonant interaction with the large-amplitude harmonic disturbance. Would therefore a pulse containing only subharmonic frequencies be more effective at triggering nonlinear subharmonic resonance with the large-amplitude harmonic disturbance than a pulse that does not contain the subharmonic part of the spectrum? Or in other words, are low-frequency perturbations ‘more dangerous’ than high-frequency perturbations and lead to vortex ejection farther upstream? An answer to these questions is sought with simulation Cases 6 and 7 where the forced wall jet from Case 2 is additionally forced with pulse type 2 or 3, respectively. As seen from figure 3(*b*), pulse type 2 in Case 6 has its amplitude peak at $f_p = 1/2$ with the main frequency band ranging from $f = 0$ to 1, whereas pulse type 3 in Case 7 has its peak at $f_p = 3/2$ with the frequency band ranging from $f = 1$ to 2. The results from simulation Cases 6 and 7 (figure 13) seem surprising at first. When comparing the respective frequency spectra in figures 13(*a*) and 13(*b*), resonant growth of the subharmonic is significantly weaker for the low-frequency pulse from Case 6 (figure 13(*a*)) than for the high-frequency pulse from Case 7 (figure 13(*b*)). Whereas in Case 6, the greatest flow response to the pulse is initially at subharmonic frequencies, the subharmonic disturbances within the wave packet are (linearly) strongly damped near the forcing location. Resonant growth only sets in at $x \approx 30$ where the subharmonics have already decreased in amplitude by an order of magnitude. In Case 7, on the other hand, the pulse generates the greatest flow response at $f \approx 3/2$, a part of the spectrum that is linearly amplified. Disturbances at subharmonic frequencies ($f \approx 1/2$), while deliberately excluded from the spectrum of the forcing pulse ($f_p = 3/2$), are inadvertently generated owing

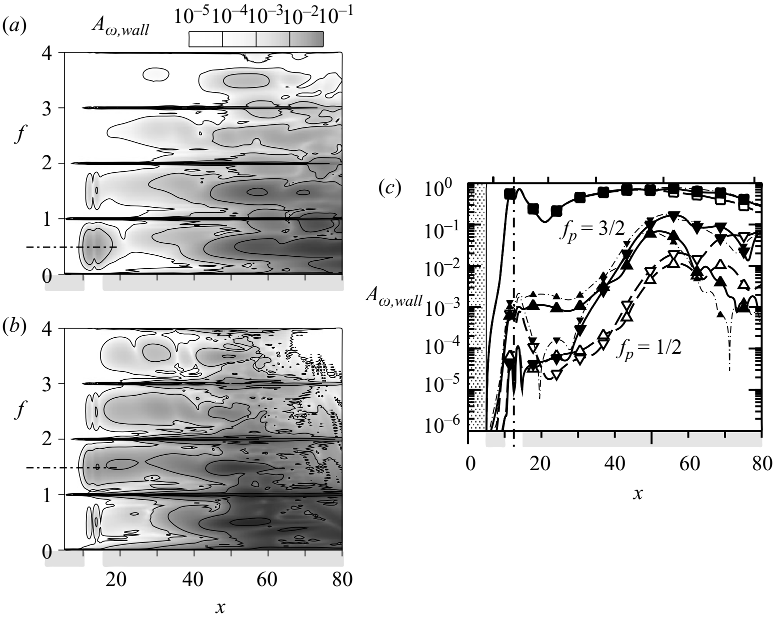

FIGURE 13. Low-frequency versus high-frequency pulse disturbance. The Fourier amplitude of the walls vorticity. (*a*) Frequency spectrum for Case 6, pulse with $f_p = 1/2$; (*b*) spectrum for Case 7, pulse with $f_p = 3/2$; (*c*) Fourier amplitude versus x for selected frequencies, $f = 1/2$ (∇); $f = 1$ ($\square$); $f = 3/2$ ($\triangle$); with curves for Case 6 marked by open symbols, for Case 7 by solid symbols, and for Case 5 (also shown for reference) by grey symbols.

to nonlinear resonant interaction with the large-amplitude harmonic disturbance ($f_h = 1$) and quickly surpass disturbances with higher frequencies in amplitude.

The initial ‘boost’ in amplitude that the subharmonic receives in Case 7 owing to the presence of the larger-amplitude higher harmonic is clearly seen from the direct comparison of Cases 6 and 7 in figure 13(*c*), plotting Fourier amplitudes of wall vorticity for frequencies $f = 1/2$, 1 and 3/2. Because of the nonlinear interaction between $f = 1$ and 3/2, the amplitude of the subharmonic in Case 7 is already one order of magnitude larger than in Case 6 at the beginning of the secondary resonant growth region downstream of $x \approx 30$. Since the secondary amplification rate during resonance is nearly identical in both cases, the subharmonic in Case 7 retains its head start and reaches nonlinear saturation much farther upstream at $x \approx 55$, compared to $x \approx 75$ in Case 6. Another indication of the importance of the higher harmonics ($f \approx 3/2$) for the onset of resonant growth is found by comparing the Fourier amplitudes in Case 7 with those of the broad-spectrum pulse in Case 5, which are also plotted in figure 13(*c*) for comparison (marked by grey symbols). Over the blowing and suction slot, upstream of the onset of secondary disturbance growth, the Fourier amplitude for $f = 3/2$ is nearly identical in both cases, whereas the Fourier amplitude for $f = 1/2$ in Case 5 exceeds that in Case 7 by an order of magnitude and is very close to that in Case 6. Yet, despite this initial discrepancy in the amplitude level of the subharmonic, the secondary resonant growth behaviour in Cases 5 and 7 is similar for both $f = 1/2$ and $f = 3/2$. This leads to the conclusion that it is the amplitude level of the higher harmonic upstream that determines the amplitude of the subharmonic during secondary resonant growth farther downstream.

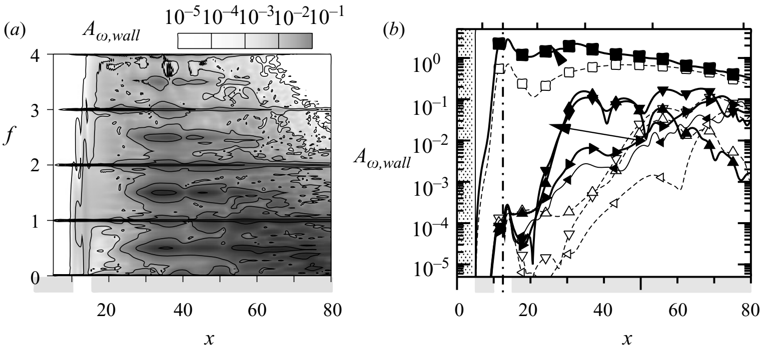

FIGURE 14. Downstream development of the wave packet in a wall jet that is forced with a very large amplitude (Case 8). (*a*) Fourier spectrum of the wall vorticity over x; (*b*) Fourier amplitude versus x for selected frequencies, $f = 1/4$ ($\triangleleft$); $f = 1/3$ ($\triangleright$); $f = 1/2$ ($\triangledown$); $f = 1$ ($\square$); $f = 3/2$ ($\triangle$). Comparison with Case 3 (Case 8, solid lines/solid symbols; Case 3, dashed lines/open symbols).

Our numerical experiments demonstrate that the nonlinear resonance mechanism in the wall jet not only involves interactions between large-amplitude fundamental ($f_h = 1$) and subharmonics ($f \approx 1/2$), but that higher harmonics ($f \approx 3/2$) are an important participant as well. Thus, the scenario leading to a more rapid onset of subharmonic resonant growth is a triad comprising the large-amplitude fundamental, f_h=1, small-amplitude higher harmonics, $f \approx 3/2$, which are linearly amplified, and smaller-amplitude subharmonics, $f \approx 1/2$, which are linearly damped, but are the recipient of nonlinear energy transfer from the larger-amplitude partners of the triad.

3.6.3. *Wave packet development for fundamental disturbance with very large amplitude*

Another important characteristic of the subharmonic resonance mechanism is its strong dependence on the amplitude of the primary disturbance. This dependence is explored using Case 8, where the forcing amplitude for the time-harmonic fundamental is increased four-fold when compared to the previous cases in our study, while the same broad-spectrum pulse is applied as in Case 3 (see table 2). Figure 14(*a*) shows the frequency spectrum of the wall vorticity for Case 8. When compared to the spectrum for Case 3 from figure 11(*a*), resonant amplitude growth in the upstream part ($x < 35$) is far stronger and, as a result, nonlinear saturation of the subharmonic pulse spectrum ($f \approx 1/2$) is also reached significantly farther upstream (at $x \approx 35$ for Case 8 versus at $x \approx 55$ for Case 3). Figure 14(*b*) provides a direct comparison of the Fourier amplitudes from Cases 8 and 3 for selected frequency components within the disturbance spectra. The figure clearly shows that the presence of a much larger primary disturbance in Case 8 than in Case 3 results in a large increase in the amplification rate for frequency components $f = 1/2$ and $3/2$. Disturbance growth is also increased for the lower frequency $f = 1/4$. However, in Case 8 it is frequency component $f = 1/3$ that reaches saturation first and surpasses component $f = 1/2$ in amplitude downstream of $x \approx 70$. Farther downstream, the subharmonic spectrum shifts to lower and lower frequencies in discrete jumps, associated with the repeated merging of vortex pairs inside the flow field. This is seen from the space–time diagram in figure 15(*a*) and the snapshots of the flow field in figure 15(*b*), where a series of subsequent vortex mergings, a 'subharmonic cascade', can be observed downstream of $x = 50$. The dipole that eventually lifts off at $x \approx 74$ and $t - t_p = 21$ comprises five

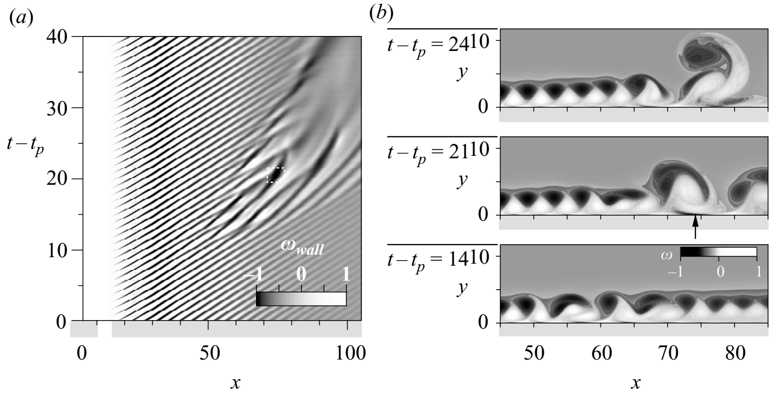

FIGURE 15. Ejection process in a wall jet that is forced with a very large amplitude (Case 8); (*a*) space–time diagram of the wall vorticity with the region of ejection marked by dashed box; (*b*) snapshots of the repeated vortex mergings before and during the vortex ejection.

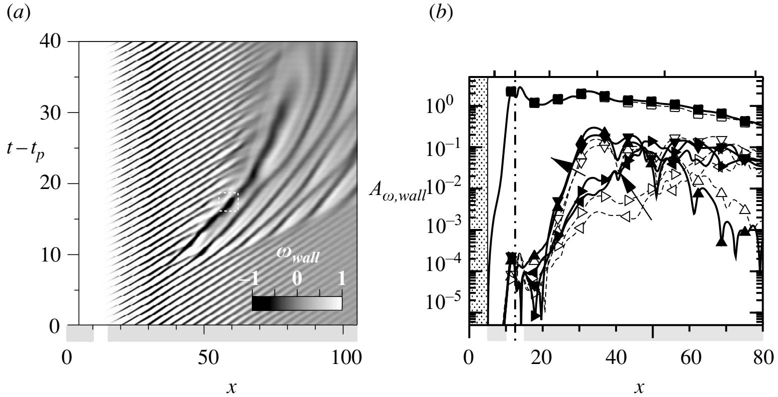

FIGURE 16. Downstream development of the wave packet in response to phase shifted pulse (Case 9); (*a*) space–time diagram of the wall vorticity with the region of ejection marked by dashed box; (*b*) Fourier amplitude versus x for selected frequencies $f = 1/4$ (◁); $f = 1/3$ (▷); $f = 1/2$ (▽); $f = 1$ (□); $f = 3/2$ (△). Comparison with Case 8 (Case 9, solid lines/solid symbols; Case 8, dashed lines/open symbols).

merged vortex pairs, then continues to ingest vortex pairs as it slowly moves away from the wall. While the complex sequence of vortex mergings makes a spectacular visual display, what is most interesting in Case 8 is the significant gap of $\Delta x \approx 20$ between the location where the subharmonic $f = 1/2$ reaches saturation ($x \approx 35$, figure 14(*b*)) and the location where the vortex mergings start to take place ($x \approx 55$, figure 15(*a*)). Without this gap (which is not observed in any of the previous cases), the vortex ejection process in Case 8 would surely occur even farther upstream.

It must be emphasized that the disturbances in Case 8 are highly nonlinear and the observed mergings occur in rapid succession. Therefore, the resonant interactions are complicated by a strong sensitivity to the phase of the disturbances, particularly for the secondary vortex pairings. Specifically, in addition to the amplitude and spectral composition of the pulse, the phase angle, $\theta_{h,p}$, (equation (2.6)) of the fundamental disturbance at the time of pulse deployment, t_p, also affects the merging sequence and the lift-off. This is demonstrated with Case 9 where the pulse is applied at $\theta_{h,p} = \pi$

(see table 2). As seen from the space–time diagram for Case 9 in figure 16(*a*), the first vortex merging is now observed at $x \approx 40$, $\Delta x = 15$ farther upstream than for Case 8 and the secondary mergings occur in a sequence that is significantly different from Case 8 in figure 15(*a*), resulting in an upstream shift of the ejection location to $x \approx 59$. The amplitude plot in figure 16(*b*) comparing Case 9 with Case 8 for selected frequencies reveals a slight upstream shift in the onset of resonant growth for frequency components $f = 1/2$ and $3/2$. Remarkably, this results in twice the saturation level for these frequencies in Case 9 (leading to the observed upstream shift in the vortex mergings) and, as a consequence, also results in stronger growth for the lower-frequency components, $f = 1/4$ and $1/3$.

The initial phase angle of the wave packet relative to the harmonic primary disturbance, and thus the onset of resonant growth, is closely connected to the receptivity process and depends on the particular forcing method for generating the pulse (i.e. slot location, slot width, blowing profile, etc.) as well as the primary disturbance itself. For resonant interaction between the primary disturbance and the prototypical pulse chosen here, the phase angle $\theta_{h,p} = 0$ proves to be favourable in Cases 3–7 and unfavourable in Case 8 leading to a delay in the onset of resonant growth. We can therefore expect that the relative phase of a small perturbation that may occur naturally in a laminar wall jet (in addition to the amplitude and frequency content of the perturbation) significantly impacts the resonant growth behaviour of the generated wave packet and ultimately also the ejection location.

3.6.4. *Vortex ejections in response to different pulse disturbances*

With Cases 3–9, various parameters influencing the nonlinear resonant interaction between a large-amplitude primary disturbance and a small-amplitude pulse disturbance have been explored, such as the amplitude and frequency content of the pulse disturbance, the amplitude of the primary disturbance and the relative phase angle between the pulse and the primary disturbance. In all these cases, owing to resonant interaction with the time-harmonic primary disturbance, the subharmonic frequency components within the generated wave packet undergo rapid amplification until, eventually, nonlinear saturation is reached, vortex mergings occur and one or multiple vortex pairs lift off from the wall. Figure 17 provides a compilation of the flow fields from Cases 4–9 at time $t - t_p = 40$ after the pulse has been introduced (Case 3 is shown in figure 7(*d*)). In each case, an arrow marks the streamwise location of the negative vorticity spike indicating the lift-off of the vortex pair. The flow fields from Cases 4 and 5 with a small and a large pulse amplitude (figures 17(*a*) and 17(*b*)) demonstrate that an increase in the pulse amplitude leads to an upstream shift in the ejection location. In Case 3, vortex lift-off occurs at $x \approx 85$ (figure 9), in between those of Cases 4 and 5. Recall from figure 12 that although the growth rate during resonance is (nearly) identical in all three cases, the larger the initial amplitude of the pulse, the farther upstream the wave packet reaches nonlinear saturation. Similarly, as seen by comparing the flow fields from Cases 6 and 7 (figures 17(*c*) and 17(*d*)), nonlinear saturation and ejection occurs farther upstream for the pulse in Case 7, with a spectrum containing frequencies to which the flow is more receptive ($f \geqslant 1$). We have seen from figure 13(*c*) that the resonant growth behaviour in Cases 5 and 7 is very similar. As a result, the flow fields in figures 17(*b*) and 17(*d*) for these cases also bear a great resemblance to each other. Lastly, the flow fields from Cases 8 and 9 (figures 17(*e*) and 17(*f*)) show that the ejection location shifts farther upstream for a larger primary disturbance amplitude and, even more so, for a favourable phase angle of the pulse relative to the primary disturbance.

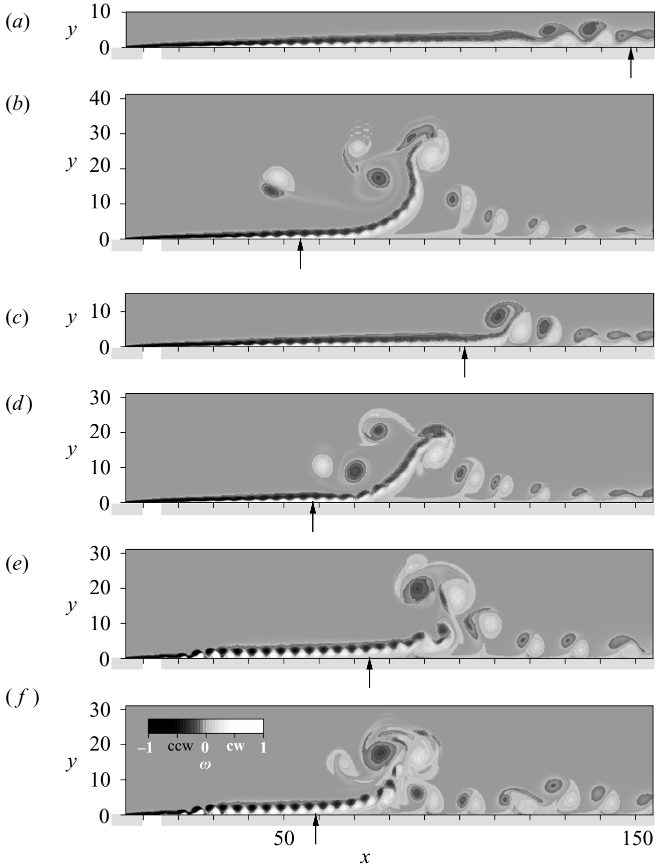

FIGURE 17. Flow response to different pulse disturbances. Grey scales of instantaneous vorticity at $t = 40$ for Cases 4–9; (*a*) small-amplitude, broad-spectrum pulse, Case 4; (*b*) large-amplitude, broad-spectrum pulse, Case 5; (*c*) low-frequency pulse, Case 6; (*d*) high-frequency pulse, Case 7; (*e*) broad-spectrum pulse with larger-amplitude fundamental, Case 8; (*f*) phase shifted broad-spectrum pulse with larger-amplitude fundamental, Case 9. Animations of Cases 4–9 are provided in movies 2–4 available with the online version of the paper.

The dependence of the ejection process on the forcing parameters is summarized in the semi-logarithmic diagram of figure 18. Plotted for pulse types 1–3 is the streamwise location of the negative vorticity spike as a function of the pulse amplitudes. Ejection locations corresponding to simulation Cases 3–9 are labelled with the respective case number. The trends that have been established for these cases are consistently observed over a wide range of pulse amplitudes: (i) the ejection location shifts upstream with increased pulse amplitude; (ii) a high-frequency pulse leads to ejection farther upstream than a low-frequency pulse; and (iii) a larger-amplitude primary disturbance also moves the ejection location farther upstream; (iv) an unfavourable relative phase angle between the harmonic and the pulse disturbance delays the ejection process for all pulse amplitudes. In fact, the phase-angle variation leading to a downstream shift of the ejection location in Case 8 compared to Case 9 has been extended to a total of ten cases with $\theta_{h,p} = 0$ to $9/5\pi$ over one fundamental oscillation cycle. While the ejection locations for phase angles $\theta_{h,p} = 2/5\pi$ to $6/5\pi$ virtually coincide at $x \approx 59$, for other angles within the cycle the ejection location

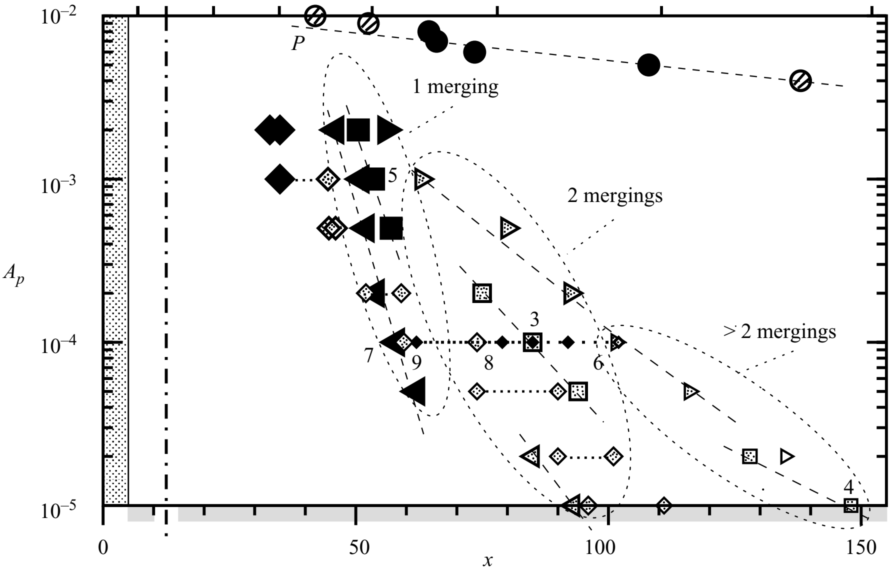

FIGURE 18. Ejection location (indicated by negative vorticity spike) for different pulse types and pulse amplitudes; broad-spectrum pulse, Cases 3–5 ($\square$); low-frequency pulse, Case 6 ($\triangleright$); high-frequency pulse, Case 7 ($\triangleleft$); broad-spectrum pulse with larger-amplitude fundamental, Cases 8 and 9 ($\Diamond$); broad-spectrum pulse alone, Case P ($\circ$). Filled symbols indicate one merging preceding the ejection; dark-shaded symbols, two mergings; light-shaded symbols, more than two mergings.

shifts downstream, farthest for $\theta_{h,p} = 9/5\pi$ to $x = 102$. Also plotted in figure 18, for reference, are the ejection locations of vortex pairs developing from a broadband pulse in the absence of a harmonic primary disturbance. Clearly, without the presence of a large-amplitude primary disturbance, the pulse amplitude must be much greater for the ejection to occur. For example, to trigger a vortex ejection at the same location as in Case 3, a pulse amplitude 60 times larger is required.

The entries in figure 18 have been marked according to the number of vortex mergings that precede the ejection process in each case. Ejections that occur farthest upstream are preceded by a single merging (filled symbols) whereas ejections farther downstream are preceded by multiple mergings (shaded symbols). Notice that within each grouping, the ejection location gradually shifts downstream as the pulse amplitude, A_p, decreases. Larger jumps between ejection locations generally coincide with an increase in the number of vortex mergings before ejection.

Whereas it is conceivable that in two-dimensional simulation of a laminar wall jet, vortex ejection occurs at some location far downstream even for exceedingly small perturbations, the wall jet in three-dimensional simulations eventually transitions to turbulence because of the presence of three-dimensional perturbations in the flow. Therefore, the underlying two-dimensional resonance mechanism promoting the ejection of vortex pairs is in competition with three-dimensional mechanisms which may counteract this ejection process.

4. Three-dimensional simulation results

Even at the moderately low Reynolds number of the laminar Glauert wall jet considered in the present study, the flow transitions to turbulence within a certain streamwise distance depending on the perturbations that are introduced into the flow. In experiments, transition may be triggered, for example, by free-stream turbulence and/or surface roughness. In numerical simulations, three-dimensional perturbations may be introduced deliberately through forcing, or may develop from numerical round-off. Nonlinear resonant interactions of these three-dimensional perturbations with 'two-dimensional' (spanwise) primary disturbances then lead to breakdown to turbulence. The current understanding of the three-dimensional stages of wall jet transition is fragmentary with only a few experimental and numerical investigations of the three-dimensional transition mechanisms reported in the literature (Bajura & Catalano 1975; Gogineni & Shih 1997; Wernz & Fasel 1997; Visbal, Gaitonde & Gogineni 1998; Levin *et al.* 2005). A detailed systematic study of these three-dimensional mechanisms with a combined numerical/experimental approach would surely be worth while. The present objective, however, is only to demonstrate the impact of three-dimensional random perturbations on the vortex ejection process that is such a prominent feature in two-dimensional simulations. Can a wave packet generated by a two-dimensional pulse disturbance overcome three-dimensional disturbances with a comparable amplitude level and thus lead to the ejection of dipolar vortices during wall jet transition?

Since the computational cost of three-dimensional direct numerical simulations exceeds the cost of two-dimensional simulations by orders of magnitude, we have limited our focus on simulation Case 2 (table 2) which was recomputed with the three-dimensional version of our Navier–Stokes code (Meitz & Fasel 2000). The computational domain employed in the two-dimensional simulations (figure 1) has been shortened to 1601 grid points in the streamwise direction with the outflow boundary now placed at $x_{out} = 205$ while all other computational parameters are kept unchanged. In the spanwise direction, a large domain size of $L_z = 40$ has been afforded and resolved using 256 collocation points. The computational grid, therefore, totals more than 73 million collocation points, well beyond the capabilities of the local computational resources employed for our two-dimensional simulations. Hence, the three-dimensional simulations have been performed on the Cray X1 supercomputer at the Army High Performance Resource Center (AHPCRC) using 32 multi-streaming processors with MPI parallelization.

4.1. *Transition of a forced wall jet in the presence of three-dimensional white noise*

In addition to harmonic two-dimensional forcing, which is identical to that from Case 2, small-amplitude white-noise disturbances are introduced in all spanwise Fourier components through the same blowing and suction slot. For generating the white-noise disturbances, a random number generator, RAN1, by Press *et al.* (1989) is employed. The amplitude level of the white noise is deliberately kept uniformly constant at $A_r = 5 \times 10^{-5}$ so that no localized wave packets are likely to be generated by the forcing. During start-up of the three-dimensional simulation, the buffer domain is initially placed near the blowing and suction slot, then moved downstream in several steps; this same strategy for damping out the start-up vortex was also used in our two-dimensional simulations. After a transient of five flow-through times, the flow field reaches a statistically stationary state (figure 19). In the upstream part of the computational domain, up to $x \approx 70$, the flow closely resembles that of the two-dimensional simulation Case 2. Farther downstream, the primary disturbances disintegrate, the flow starts to spread rapidly in the wall-normal direction and appears to be dominated by random fluctuations. The rapid increase in the wall-jet spreading downstream of $x = 70$ is seen from the development of the half-width (thick dashed line in figure 19) which increasingly deviates from its original development for the unperturbed laminar flow (thin dashed line). As the flow transitions, the streamwise mean velocity, also plotted in figure 19 for three streamwise locations, changes shape from a laminar Glauert profile at $x = 50$ to approach a turbulent profile at $x = 150$.

4.2. *Vortex ejection during wall-jet transition*

The flow response to two different pulse disturbances is now investigated: (i) the broad-spectrum pulse from Case 3 (type 1, figure 3) and (ii) the high-frequency pulse from Case 7 (type 3, figure 3). In both cases, the pulse amplitude ($A_p = 10^{-4}$) rises above the amplitude level of the random disturbances ($A_r = 5 \times 10^{-5}$) and the pulse therefore represent a localized event within a uniformly random background noise. Not surprisingly, a pulse of smaller amplitude is ‘drowned out’ by the background noise and does not generate a noticeable flow response. On the other hand, the pulse amplitude is only moderately larger than the background and the occurrence of such localized perturbations in the natural flow can be easily conceived. Figures 20(*a*) and 20(*b*) show the flow fields from the three-dimensional simulation Cases 3 and 7 at time $t = t_p + 40$ after the pulse has been introduced in each case. The corresponding two-dimensional simulations are shown in figures 7(*d*) and 17(*d*). Clearly, for both cases a strongly amplified wave packet has developed in response to the pulse. However, the wave packet in Case 3 does not disrupt the three-dimensional transitional flow enough to cause a vortex ejection, which occurs at $x = 85$ in the two-dimensional simulation. Evidently, the three-dimensional fluctuations associated with the onset of transition have a weakening effect on the spanwise vortex pairs. For Case 7, on the other hand, where the vortex ejection occurs at $x = 59$ in the two-dimensional simulation, a massive counter-clockwise rotating vortex is situated above the flow and the jet underneath is lifted away from the wall. The clockwise rotating vortex that is part of the ejected dipole observed in two-dimensional simulations has been shredded by the strong three-dimensional disturbances that emerge during transition.

Further details of the ejection process in the three-dimensional simulation of Case 7 are revealed in figure 21 which shows snapshots at four time instants of the three-dimensional vortical structures inside the flow field represented by the Q-criterion according to Hunt, Wray & Moin (1988). Q is defined as

$$Q = \tfrac{1}{2}(W_{ij}W_{ij} - S_{ij}S_{ij}) \tag{4.1}$$

and thus identifies flow regions where rotation, W_{ij}, exceeds strain, S_{ij}. The snapshots of the vortical structures at time $t = t_p$ (figure 21(*a*) and $t = t_p + 40$) figure 21(*d*) directly correspond to the grey-scale plots of spanwise vorticity in figures 19 and 20(*b*), respectively. Although Q cannot distinguish between clockwise and counterclockwise rotating vortices, it nicely illustrates the development from the two-dimensional disturbances in the upstream part of the flow, to the emergence of spanwise modulations, to the highly complex three-dimensional intertwined vortical structures during turbulent breakdown in the downstream part of the computational domain. The snapshot at $t = t_p + 20$ in figure 21(*b*) captures the vortex dipole as it starts to lift away from the wall just upstream of the region of three-dimensional turbulent breakdown. Although noticeably distorted by spanwise modulations, the vortex pair is still highly coherent. At $t = t_p + 25$, as illustrated by figure 21(*c*), strong streamwise vortical structures have developed that wrap around the vortex pair. The snapshot

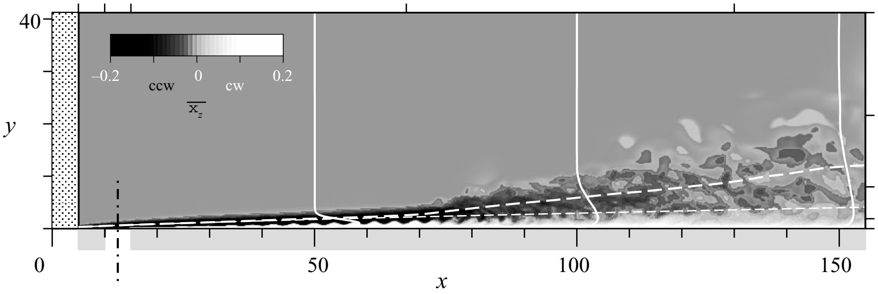

FIGURE 19. Direct numerical simulation of transition in a Glauert wall jet triggered by blowing and suction with a two-dimensional large-amplitude harmonic perturbation and with three-dimensional small-amplitude white noise (Case 2). The spanwise average of spanwise vorticity and superposed streamwise mean velocity profiles is shown at three streamwise locations. Also shown is the half-width of the transitional wall jet and the half-width of the initially undisturbed two-dimensional Glauert wall jet (base flow).

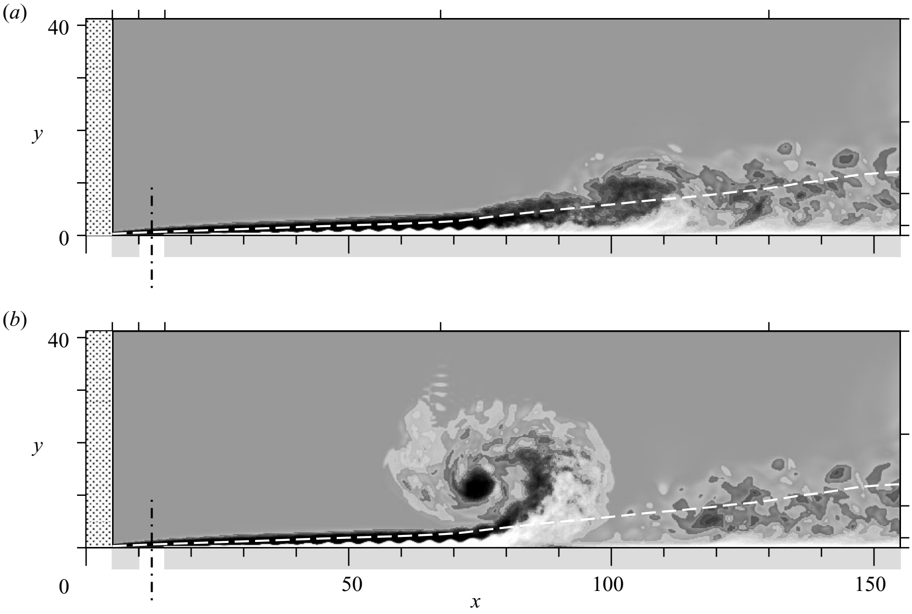

FIGURE 20. Transitional wall jet subjected to two different pulse disturbances. Snapshots of the flow field (spanwise average of spanwise vorticity) are shown at time $t = t_p + 40$; (a) broad-spectrum pulse (type 1, Case 3); (b) high-frequency pulse (type 3, Case 7).

at $t = t_p + 40$ in figure 21(d) depicts the counterclockwise rotating spanwise vortex (compare with figure 20(b)) encased in a tangle of three-dimensional vortical structures that have disintegrated its clockwise-rotating counterpart within the vortex pair. Clearly, the rapidly growing wave packet in Case 7 succeeds in 'pealing' the jet off the wall before the vortex pairs within the primary disturbance lose their spanwise coherence owing to the emergence of three-dimensional vortical structures during turbulent breakdown.

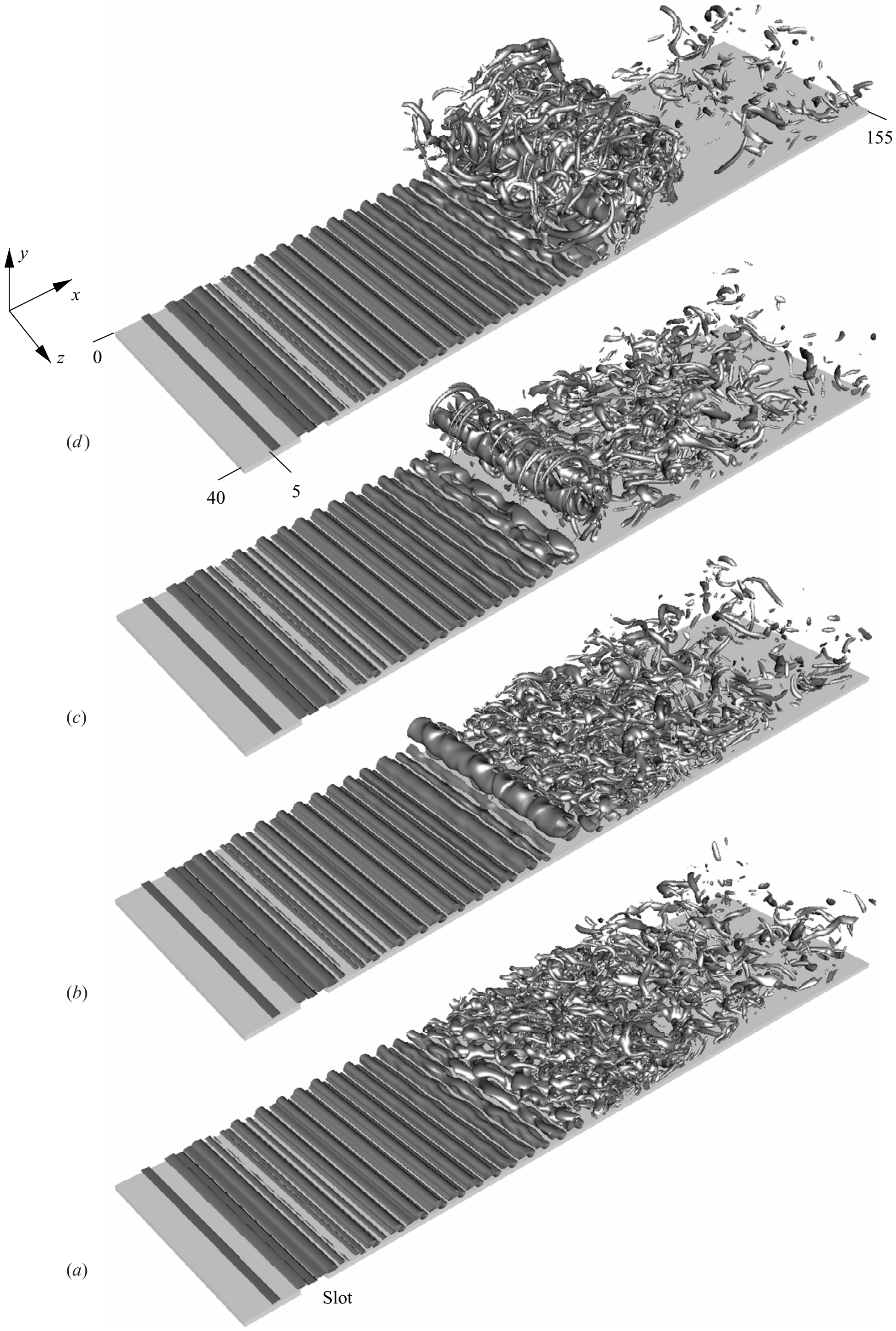

FIGURE 21. Ejection of dipolar vortex in the transitional wall jet in response to high-frequency pulse (type 3, Case 7). Vortical structures represented by iso-surfaces of $Q = 0.002$ at four time instants; (*a*) $t = t_p$, (*b*) $t = t_p + 20$, (*c*) $t = t_p + 25$, (*d*) $t = t_p + 40$, Movie 5, available with the online version of the paper shows an animation of this.

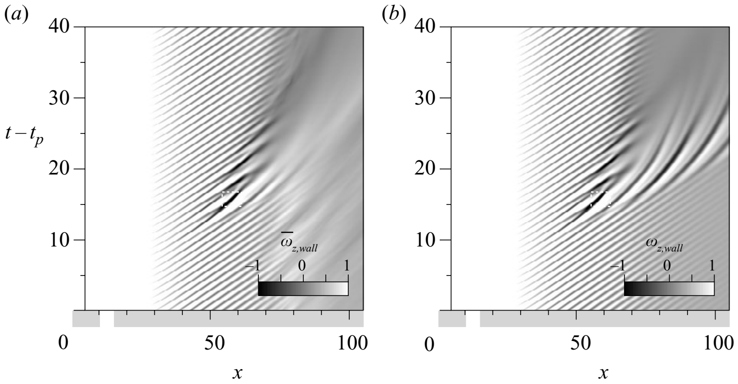

FIGURE 22. Development of a wave packet in response to a high-frequency pulse (type 3, Case 7). Space–time diagram of the spanwise-averaged spanwise wall vorticity; (*a*) three-dimensional simulation; (*b*) two-dimensional simulation.

4.3. *Development of wave packet during wall-jet transition*

The development of the wave packet leading to the vortex ejection in the three-dimensional simulation of Case 7 is documented by the space–time diagram in figure 22(*a*) of the spanwise averaged spanwise wall-vorticity, $\overline{\omega}_{z,wall}$. Also shown for comparison in figure 22(*b*) is the corresponding two-dimensional simulation of Case 7. Downstream of $x = 70$, as the flow breaks down to turbulence in the three-dimensional simulation, the imprint of the spanwise vortices in the wall vorticity is severely diminished even before the wave packet reaches nonlinear saturation. Farther upstream, however, where the flow is dominated by 'two-dimensional' spanwise coherent disturbances, the development of the wave packet including the vortex mergings before and during lift-off is virtually identical in both figures 22(*a*) and 22(*b*). In either case, the negative spike in the wall-vorticity occurs at $x \approx 58$ and $t \approx t_p + 16$ (the region marked by the dashed box) indicating the lift-off of the vortex dipole from the wall. Although the pulse amplitude in Case 7 exceeds the amplitude level of the random white-noise perturbations only by a factor of two, the wave packet development in response to the pulse is hardly influenced by three-dimensional disturbances in the flow field until ejection has taken place.

How similar the wave-packet development is in both the two- and three-dimensional simulation of Case 7 can also be seen when comparing the two-dimensional disturbance spectrum from the three-dimensional simulation in figure 23(*a*) with the spectrum from the corresponding two-dimensional simulation in figure 13(*b*). Both cases show the same strong flow response in the frequencies centred around $f = 3/2$ and the same shift towards subharmonic frequencies farther downstream owing to nonlinear resonant interaction. Additionally, over the blowing and suction slot, the Fourier spectrum for the three-dimensional simulation in figure 23(*a*) reveals a uniform flow response across the entire frequency range shown in response to the additional white-noise forcing in this case. However, the flow is not nearly as receptive to the random forcing. This is seen from figure 23(*b*) which plots the frequency spectrum for Case 2 where, in addition to the primary harmonic disturbance, the flow is forced with random white noise, but no pulse. Qualitatively, the frequency spectrum in figure 23(*b*) resembles the spectrum in figure 23(*a*), also showing the strongest flow response at $f \approx 3/2$ and $f \approx 1/2$, albeit at a far smaller amplitude. As seen from figure 23(*c*) which plots the Fourier amplitudes of selected frequency

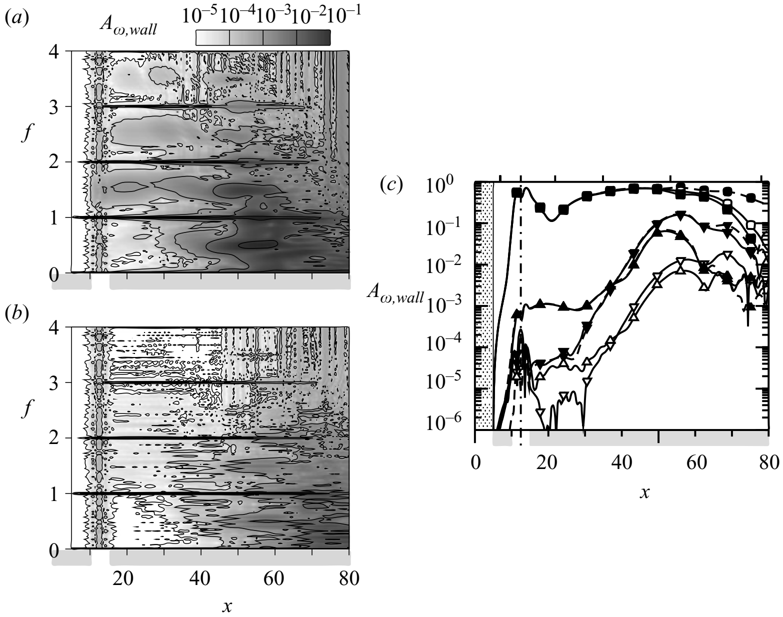

FIGURE 23. Fourier spectrum of two-dimensional disturbances during wall-jet transition (three-dimensional simulations). Shown are Fourier amplitudes of the spanwise-averaged spanwise wall vorticity versus streamwise location; (*a*) frequency spectrum for Case 7 (high-frequency pulse); (*b*) frequency spectrum for Case 2 (no pulse); (*c*) direct comparison of Fourier amplitudes from Case 2 (open symbols) and Case 7 (symbols with solid lines) for selected frequencies, $f = 1/2$ (▽); $f = 1$ (□); $f = 3/2$ (△). Also shown for comparison are the corresponding curves from the two-dimensional simulation of Case 7 (symbols with dashed lines).

components, the disturbance growth in Cases 2 and 7 is indeed very similar for both $f = 1/2$ and $f = 3/2$. However, for Case 7, the Fourier amplitude in $f = 3/2$ not only is several times larger over the blowing and suction slot (especially considering that the pulse duration, $\Delta t_p = 8$, is much shorter than the sampling period for the Fourier transform, $\Delta t_p = 40$, while the random forcing is applied throughout the interval), but more importantly, it does not decay downstream of the slot. The combined effect in Case 7 of increased forcing amplitude in $f = 3/2$ and a much higher receptivity of the flow to the pulse disturbance provides the two-dimensional wave packet with a significant ‘head start’ over other, random disturbances and thus the vortex ejection ahead of the three-dimensional breakdown is not so surprising after all.

5. Conclusion

Time-dependent two-dimensional perturbations can be highly disruptive to laminar wall jets by triggering the development of energetic counter-rotating vortex pairs from hydrodynamic instabilities. If strong enough, these dipolar vortices can lift away from the wall and, in some cases, lead to the detachment of the entire jet from the wall. In the present paper, by means of two-dimensional numerical simulations of prototypical test cases, we have systematically studied the physical mechanisms responsible for this fascinating ejection phenomenon. The simulations suggest that the following two ingredients are required for ejection to occur: (i) a disturbance that is non-periodic in time, and (ii) a large-amplitude disturbance. From a small-amplitude pulse disturbance, a downstream propagating wave packet develops which grows and decays linearly without lasting disruption of the wall jet. Time-harmonic forcing with a large disturbance amplitude leads to the development of a double row of energetic counter-rotating vortices in the inner and outer regions of the jet which reach a stable time-periodic state following a transient phase after the start-up of the forcing. When the two disturbance types are introduced simultaneously, however, nonlinear interaction leads to rapid resonant growth of the subharmonic part within the frequency spectrum of the wave packet and, as a result, the double vortex row is disrupted by vortex merging and vortex lift-off. This model scenario is a prototype for the early two-dimensional stages of transition in a laminar wall jet, in particular when the flow is forced periodically in time and when, because of the presence of large-amplitude harmonic disturbances, wave packets developing from low-level two-dimensional background perturbations experience rapid resonant growth. Of course, distinct energetic vortex pairs can also be produced directly by massive disturbances that are simultaneously non-periodic in time and large in amplitude, such as large-amplitude pulse disturbances, disturbances generated during an abrupt start-up of blowing or of forcing with a large amplitude.

Whereas in two-dimensional numerical simulations the forced laminar wall jet is dominated by the subharmonic resonance mechanism and vortex ejections are difficult to prevent, in three-dimensional simulations, or in nature, the wall jet eventually breaks down to turbulence and the two-dimensional subharmonic resonances are in competition with three-dimensional resonances during the transition process. As shown with a three-dimensional direct numerical simulation, where the laminar wall jet is forced by small-amplitude white noise in addition to the large-amplitude time-harmonic forcing, three-dimensional perturbations lead to the breakup of the double-vortex row into three-dimensional turbulent motion within a certain streamwise distance. In this transitional flow, a two-dimensional pulse disturbance can still trigger a vortex ejection if the generated two-dimensional wave packet reaches a large amplitude upstream of the turbulent breakdown region. However, the simulations also indicate that for this to occur, the pulse amplitude must be at least moderately larger than the amplitude level of the three-dimensional perturbations. It is easily conceivable that in a laminar wall jet with a low turbulence level, such two-dimensional time-local perturbations indeed occur at times, and the vortex ejections in the experiments by Bajura & Catalano (1975) provide an indication of this. The mixture of two- and three-dimensional perturbations introduced upstream into the laminar wall jet and the receptivity of the flow to these perturbations therefore strongly affect whether vortex ejection will occur or not as a possible outcome of the competition between two- and three-dimensional resonance mechanisms during wall-jet transition.

Support for this research was provided by the Air Force Office of Scientific Research under grant F49620-00-10069 and by the Office of Naval Research under grant N000014-01-0932. The three-dimensional simulations were made possible by a grant of HPC time on the Cray X1 at the Army High Performance Research Center.

REFERENCES

Ahlnäs, K., Royer, T. C. & George, T. H. 1987 Multiple dipole eddies in the Alaska coastal current detected with landsat thermatic mapper data. *J. Geophys. Res.* **92**, 13 041.

Bajura, R. A. & Catalano, M. R. 1975 Transition in a two-dimensional plane wall jet. *J. Fluid Mech.* **70**, 773–799.

Conlon, B. & Lichter, S. 1995 Dipole formation in the transient planar wall jet. *Phys. Fluids* **7** (5), 999–1014.

Fasel, H. & Wernz, S. 1996 Numerical simulation of wall jets. In *Engineering Turbulence Modelling and Experiments 3* (ed. W. Rodi & G. Bergeles), pp. 621–630. Elsevier.

Glauert, M. B. 1956 The wall jet. *J. Fluid Mech.* **1**, 625–643.

Gogineni, S. & Shih, C. 1997 Experimental investigation of the unsteady structure of a transitional plane wall jet. *Exps. Fluids* **23**, 121–129.

Hunt, J. C. R., Wray, A. A. & Moin, P. 1988 Eddies, stream, and convergence zones in turbulent flows. CTR S88. Center for Turbulence Research.

Levin, O., Chernoray, V. G., Löfdahl, L. & Henningson, D. S. 2005 A study of the Blasius wall jet. *J. Fluid Mech.* **539**, 313–347.

Meitz, H. & Fasel, H. F. 2000 A compact-difference scheme for the Navier–Stokes equations in vorticity–velocity formulation. *J. Comput. Phys.* **157**, 371–403.

Mele, P., Morganti, M., Scibillia, M. F. & Lasek, A. 1986 Behavior of wall jet in laminar-to-turbulent transition. *AIAA J.* **24**, 938–939.

Press, W. H., Flannery, B. P., Teukolsky, S. A. & Vetterling, W. T. 1989 *Numerical Recipes, The Art of Scientific Computing (Fortran Version)*. Cambridge University Press.

Tsuji, Y., Morikawa, Y., Nagatani, T. & Sakou, M. 1977 The stability of a two-dimensional wall jet. *Aero. Q.* **28**, 235–246.

Tumin, A. 1998 Subharmonic resonanance in a laminar wall jet. *Phys. Fluids* **10** (7), 1769–1771.

Tumin, A. & Aizatulin, L. 1997 Instability and receptivity of laminar wall jets. *Theor. Comput. Fluid Dyn.* **9**, 33–45.

Visbal, M. R., Gaitonde, D. V. & Gogineni, S. P. 1998 Direct numerical simulation of a forced transitional plane wall jet. *AIAA Paper* 98-2643.

Wernz, S. 2001 Numerical investigations of forced transitional and turbulent wall jets. PhD thesis, The University of Arizona.

Wernz, S. & Fasel, H. F. 1996*a* Numerical investigation of unsteady phenomena in wall jets. *AIAA Paper* 96-0079.

Wernz, S. & Fasel, H. F. 1996*b* Vortex motion in an unsteady forced wall jet. *Phys. Fluids* **8** (9), S11.

Wernz, S. & Fasel, H. F. 1997 Numerical investigation of forced transitional wall jets. *AIAA Paper* 97-2022.

Wernz, S. & Fasel, H. 2000 Numerical investigation of resonance phenomena in wall jet transition. In *Laminar – Turbulent Transition – IUTAM Symposium Sedona/AZ 1999* (ed. H. F. Fasel & W. S. Saric), pp. 217–222. Springer.

Zhou, M. D., Rothstein, J. & Wygnanski, I. 1992 On the hydrodynamic stability of the wall jet. *Eleventh Australian Fluid Mechanics Conference, Hobart, Australia*.